Structural analysis of *Spiroplasma* cytoskeletons by using electron microscope

（電子顕微鏡を用いたスピロプラズマの細胞骨格の構造解析）

理学研究科

生物地球系専攻

令和 4 年度

Yuya SASAJIMA

（笹嶋 雄也）

CONTENTS

ABBREVIATIONS AND ACRONYMS

I use these abbreviations and acronyms in this thesis as follow.

2D: two-dimensional

3D: three-dimensional

ATP: adenosine 5’-triphosphate

AdoHcy: S-adenosyl-L-homocysteine

BLAST: basic local alignment search tool

CCCP: carbonyl cyanide m-chlorophenyl hydrazine

CCD: charge-coupled device

CMOS: Complementary Metal-Oxide Semiconductor

CTF: contrast transfer function

DTT: (+/-)-dithiothreitol

EM: electron microscope/microscopy

ET: electron tomography

HEPES: 4-(2-hydroxyethl)-1-piperazineethanesulfonic acid

LH: left-handed

MALDI-TOF: matrix assisted laser desorption/ionization-time of flight

MC: methylcellulose

MTA: methylthioadenosine

PBS: phosphate-buffered saline

PDB: protein data bank

PG: peptidoglycan

PMSF: phenylmethylsulfonyl fluoride

QFDE: quick-freeze, deep-etch

RH: right-handed

SAH: S-adenosylhomocysteine

S.D.: standard deviation

SDS-PAGE: sodium dodecyl sulfate polyacrylamide gel electrophoresis

TEM: Transmission electron microscope/microscopy

Tris: 2-amino-2-hydroxymethyl-propane-1,3-diol

GENERAL INTRODUCTION

Spiroplasma

Spiroplamsa is a helical shaped bacterial which lacks a peptidoglycan layer. They are mostly commensal to various hosts, primarily arthropods and plants, and has been isolated from everywhere all over the world. *Spiroplasmas* sometimes cause serious disease by the infection to those hosts. *S. citri* is known as the pathogen of citrus stubborn disease in which Spiroplasma cells infect citrus fruits and cause deformities of the wood and fruit, resulting in reduced yields. Another *spirplasma*, *S. kunkelli* is also known as the pathogen of corn stunt disease in which *Spiroplasma* cells infect corn and cause corn to mature small, resulting in reduced yields. In the infection procedure of the corn stunt disease, leafhopper is also known to work as a transmitter of *Spiroplasma* cells to corn. Since these *Spiroplasma* infectious disease cause serious economic damages, understanding and corresponding to these infections are urgent. Such wide spreading host-to-host interactions and virulence may possibly be due to a characteristic swimming motility of *Spiroplasma*. Interestingly, *Spiroplasma* can swim by a unique mechanism that is unrelated to the flagellar or pili motility common in general bacteria. That is, they can propel in a media by alternately switching their helical cell body between right- and left-handed. The unique swimming of *Spiroplasma* is driven by their internal structure called ribbon. The ribbon is possibly composed of bacterial actin MreB and *Spiroplasma* specific Fibril protein.

Bacterial actin MreB

MreB, a homolog of eukaryotic actin, is one of the bacterial cytoskeletal proteins. Like actin, it shows polymerization and depolymerization dynamics using energy generated by ATP hydrolysis. MreB also has a unique membrane binding site and MreB filament localizing on cell membrane has been observed. In bacteria which have a cell wall consist of peptidoglycan layer such as E. coli and B. subtilis, MreB is known to function as a scaffold for the peptidoglycan synthesis. On the other hand, the role of MreB in *Spiroplasma* which have no peptidoglycan has long been a mystery. Previous study suggested that MreB filament localize the innermost line of the helical cell body as a part of the protofilaments that compose the ribbon structure. Furthermore, recent studies have also revealed that MreB functions as a cytoskeleton which plays an important role in the helical cell formation and as a motor protein for force generation involving the swimming motility in *Spiroplasma*. In this thesis, I discuss the mechanism of force generation by MreB in *Spiroplasma* swimming motility.

Cytoskeletal Fibril

Fibril protein, with a molecular weight of 59 kDa, is a cytoskeletal protein conserved only in *Spiroplasma* species. It has been noted as a major component of the internal structure called the cytoskeletal ribbon which localizes along the innermost line of the helical cell body. Since the insoluble fraction of *Spiroplasma* cells treated with detergents contains large amounts of the Fibril filament, Fibril filaments have been isolated and performed structural analysis for a long time. In a previous study, the structural prediction by using amino acid sequences and structural analyses by electron microscopy suggests that the Fibril protein undergoes conformational changes due to autophosphorylation. Then, the Fibril protein which compose the ribbon was proposed to function as a linear motor by switching between monomeric and tetrameric states. In a proposed model for *Spiroplasma* swimming, the Fibril filaments undergoes expansion and contraction and generate a counter torque that switches the helical cell body between right- and left-handed, pushing the water backward and propelling the cell body. However, these working models were just imagination because the detailed structure of the Fibril filament is unclear. In this thesis, I performed the structural analysis by single particle analysis represented by cryo-EM which has been incredibly developing in recent years, to clarify the detailed structure of the Fibril protein.

Bacterial S-adenosylhomocysteine (SAH) nucleosidase

SAH nucleosidase catalyzes the irreversible cleavage of 5′-methylthioadenosine and S-adenosylhomocysteine to adenine and its corresponding thioribose, 5′-methylthioribose and S 5′-methylthioribose and S-ribosylhomocysteine, respectively. This enzyme is essential for survival, mainly involved in the metabolism of AdoHcy and MTA nucleosides in bacteria. SAH nucleosidase is not present in mammalian cells, which makes this enzyme an attractive target for antibiotics against bacterial infections. Interestingly, The Fibril protein is evolutionarily derived from the nucleosidase, and the amino acid sequence corresponding to the N-terminal domain of the Fibril protein shows similarities to those of nucleosidases. The structural studies of the SAH nucleosidase have been actively performed in terms of inhibitors binding to the active site. Therefore, the structural comparison between the nucleosidase and the Fibril protein may lead to the development of further effective drugs against the *Spiroplasma* infections. From this perspective, it is also important to clarify the detailed structure of the Fibril protein.

CHAPTER I

Prospects for the mechanism of *Spiroplasma* swimming

Keywords: helix, MreB, fibril protein, SAH nucleosidase, electron microscopy, cooperativity, kink, evolution.

Abstract

Spiroplasma are helical-shaped bacteria that lack a peptidoglycan layer. They are widespread globally as parasites of arthropods and plants. Their infectious processes and survival are most likely supported by their unique swimming system, which is unrelated to well-known bacterial motility systems such as flagella and pili. *Spiroplasma* swims by switching the right- and left-handed helical cell body alternately from the cell front. The kinks generated by the helicity shift travel down along the cell axis and rotate the cell body posterior to the kink position like a screw, pushing the water backward and propelling the cell body forward. An internal structure called the “ribbon” has been focused to elucidate the mechanisms for the cell helicity formation and swimming. The ribbon is composed of *Spiroplasma-specific* fibril protein and a bacterial actin, MreB. Here, I propose a model for helicity-switching swimming focusing on the ribbon, in which MreBs generate a force like a bi-metallic strip based on ATP energy and switch the handedness of helical fibril filaments. Cooperative changes of these filaments cause helicity to shift down the cell axis. Interestingly, unlike other motility systems, the fibril protein and *Spiroplasma* MreBs can be traced back to their ancestors. The fibril protein has evolved from methylthioadenosine/S-adenosylhomocysteine (MTA/SAH) nucleosidase, which is essential for growth, and MreBs, which function as a scaffold for peptidoglycan synthesis in walled bacteria.

Introduction

Spiroplasma is a parasitic bacterium that infects arthropods and plants globally (1, 2). Their interactions with hosts are mostly commensal but sometimes pathogenic, causing economical damage to different industries (2). Interestingly, *Spiroplasma poulsonii* is known to disrupt the sex ratio of *Drosophila* species by killing males (2, 3). Their successful survival may be supported by a unique swimming mechanism, which may be advantageous for translocation in the tissues of their hosts, because they do not stack due to high load to their appendages as do flagella and pili, which are widespread in bacterial motility (4,

5). *Spiroplasma* possesses helical cell morphology and swims in viscous media by switching handedness (6, 7).

The genus *Spiroplasma* belongs to the phylum Tenericutes, comprising of the class Mollicutes, which evolved from the phylum Firmicutes represented by *Bacillus* and *Clostridium*. Mollicutes have some of the smallest genome sizes among all culturable organisms and lack a peptidoglycan (PG) layer, unlike other bacteria (5, 8, 9). These unique characteristics were established during the evolutionary process of Mollicutes from Firmicutes. Many bacterial species, including *Escherichia coli* and *Bacillus subtilis*, can grow in the L-form, which does not synthesize the PG layer under stresses inhibiting peptidoglycan maintenance (10). Mollicutes may have survived in the L-form due to their ability to escape the innate immune system of their hosts by halting the synthesis of PG, a major target of natural immune system of hosts (10). During the evolution from a Firmicutes-like ancestor to extant Mollicutes, they established stable parasitism with the acquisition of adhesion ability, modulation of antigenic properties, and reduction in metabolic pathways. In the absence of the PG, the flagella based motility common in Firmicutes was lost, because the machinery is anchored to the PG layer (5). Hence, Mollicutes may have evolved new motility systems because motility is beneficial for parasitic life. Interestingly, in addition to *Spiroplasma* swimming, class Mollicutes have two types of unique gliding motilities, even though they are a small group, as discussed previously (11, 12). The mechanism of *Spiroplasma* swimming has attracted many researchers in the fields of mycoplasmology, motility, and structural biology. Although the mechanism has been discussed in some aspects, a model for the whole image has not been emerged (1, 6, 7, 13-17). In this perspective review, I suggest a working model to explain the swimming mechanism and its evolution based on currently available information and ideas.

Main text

Swimming scheme

Spiroplasma swimming has been analyzed for three species, *Spiroplasma melliferum*, *Spiroplasma citri*, and *Spiroplasma eriocheiris* (6, 7, 13-15, 18, 19). They are characterized as a helical cell 2-10 μm long with a tapered end (Figure 1A and B) (Video 1). They swim up to 5 μm/s in viscous media by dynamically switching their handedness. The cells have different handedness simultaneously localizing along the cell axis, reversing the handedness from the tapered end, making a kink at the boundary of the axis (6, 7, 13). When the kink travels along

the cell axis, the helical structure on one side of the kink rotates in one direction, and the other side rotates in the opposite direction to counteract the torque (Figure 1B). These two directional rotations caused by the helicity shift generate a propulsion force in one direction. When the environmental viscosity increases, the swimming speed increases while maintaining the traveling speed of the kink, suggesting that the force is transmitted from helix rotation to water via friction (7). In more detail, the cell pushes water backward by rotating the backside cell body from the kink position like a propeller, and the cell progresses like a corkscrew (Figure 1B) (6). When the cell swims in one direction, the distributions of helix handedness, generation, and traveling of the kink in a cell can be presented as shown in Figure 1C (13). Note that as the cell architecture is composed of proteins, and that the structures and behaviors have intrinsic chirality not in mirror images (18).

No other motility system is driven by switching the helical handedness of a cell (4, 5). Although Spirochetes, which are a phylum of gram-negative bacteria, are also known as helical-shaped swimming bacteria, their swimming system is completely different from that of *Spiroplasma* (Figure 1D) (4, 20, 21). Spirochetes rotate and propel the cell body by rotating their flagella that are aligned along the cell axis in the periplasmic space.

Cell architecture in swimming

The characteristic helical cell shape of *Spiroplasma* is maintained by an internal ribbon approximately 150 nm wide, which runs the whole cell length (Figure 2A) (16-19). The ribbon, comprising sheets of cytoskeletal filaments, is aligned along the innermost line of the helical cell structure. It can be divided into the central zone, 30 nm wide, and outer zones based on electron microscopy (17). In the outer zone, “fibril” filaments are suggested to be aligned horizontally with 10 nm periodicity (17). Fibril protein is specific to the *Spiroplasma* genus and has been the focus of research since 1980 (Figure 2B). (16, 22, 23). Recently, the critical role of fibril filaments has been suggested, based on its structure determination using electron microscopy (18). The structure was consistent with previous works but did not suggest contraction and extension, as expected previously (17, 24). Instead, it suggested roles as the determinant of cell helicity. The fibril filament is composed of oval rings with dimensions of 11 and 6 nm, a cylindrical connecting part, and aligned with an 8.7 nm unit length (Figure 2B) (18). The units do not disassemble or change its length, however each unit is twisted either side relative to adjacent ones. The side view of the fibril filament showed that the cylindrical part formed a positive curvature (Figure 2B). In a cell, the fibril

filaments are aligned beneath the membrane with this curvature, forming parts of the ribbon (Figure 3A) (17, 18). The isolated fibril filaments showed half pitches around 350 nm similar to those of cells, suggesting that the cell helicity is determined by fibril filaments. As the helicity shift for swimming travels along the cell axis, the shift in fibril filaments likely transmits to the next subunit, probably through the strong cooperativity of fibril filaments along the ribbon axis (13), with accumulating their twists. The twists rotate the backside of the shift point, resulting in pushing the water backward (Figure 3B). In our current model, fibril filaments determine the cell helicity and its shift. Then, what generates the force for helicity shift of fibril sheet? I focus on another major components, MreB.

Filaments of *Spiroplasma* MreB, a member of the actin superfamily were suggested to associate laterally to the fibril sheet, at two different positions by two independent studies (16, 17). Here, I focus on the MreB filaments forming the inner zone of the ribbon, 30 nm wide (Figure 3A) (17). MreB, a widely conserved protein in rod-shaped bacteria, polymerizes into short antiparallel double-stranded filaments, and binds to the cell membrane (25). Although walled bacteria have only one type of MreB, all *Spiroplasma* species have five classes of MreB (14, 26, 27). Here, I refer to *Spiroplasma* MreB as SMreB because they are phylogenetically distant from those conserved in walled bacteria. In a previous study using a *S. citri* mutant with swimming defect, SMreB5 was shown to be essential for helicity formation and swimming (14, 28). It forms antiparallel double-stranded filaments and binds to both the membrane and fibril protein (Figure 2C).

The ribbon binds to a rod structure named “dumbbell”, which is about 240 nm long, at the tapered end of a cell (Figure 3A) (19). The dumbbell structure that forms the tapered end may contribute to swimming directionality. In contrast to the two types of gliding motilities in class Mollicutes (29, 30), *Spiroplasma* shows obvious chemotactic behavior toward amino acids and sugars (19). They change the swimming direction by reversing the direction of kink traveling, as well as by changing the reversal frequency (Figure 1B). Interestingly, the genes of the two-component regulatory system, involved in all chemotaxis systems of other bacteria, were not found in the *Spiroplasma* genomes. This implies that *Spiroplasma* has a completely new chemotaxis system, or that it has a two-component regulatory system distantly related to the common type. The

dumbbell may be responsible for both cell polarity and control of the swimming direction.

Possibility for force generation mechanism

Generally, bacterial motility is driven by energy from ATP or the membrane potential (5). As Mollicutes have no respiratory pathway, the energy for cell activities is thought to be supplied through ATP, which is produced by metabolic pathways (31, 32). Therefore, ATP should be more efficient as an energy source for Mollicutes motilities. In fact, two types of gliding systems, found in *M. mobile* and *M. pneumoniae*, are based on ATP energy (33-35). *Spiroplasma* swimming can be stopped by the addition of carbonyl cyanide 3-chlorophenylhydrazone (CCCP), a proton ionophore (13), suggesting that the energy for swimming is supplied from membrane potential. However, CCCP may affect other than membrane potential, because much higher concentration was required to stop the swimming. If *Spiroplasma* swimming is also driven by ATP energy as other Mollicutes motilities (33-35), SMreBs are candidates for force generators. In fact, polymerization dynamics based on ATP energy are known for conventional MreBs and SMreBs (36-38). The stability of SMreB filaments in swimming cells remains unclear. However, they are likely to retain some filaments, as supported by the binding ability of SMreB5 to fibril filaments and liposomes (14, 28).

Here, I attempt to explain the force-generation mechanism. One simple idea is that MreB molecules assembled in the ribbon perform contraction and extension through its binding reactions, which are related to the polymerization dynamics. If the individual SMreB filaments are made by a uniform SMreB isoform, they can have specific timing for contraction and extension, resulting in curve formation of a filament sheet. In more detail, an SMreB filament assembled in a ribbon can contract through subunit association, and also can extend through dissociation. This behavior is like a “bi-metallic strip,” which is made by the combination of different metals and was previously widely used for switches in electricity circuits. If the change in the curvature of the SMreB filaments is large enough, it can cause a helicity shift (Figure 4A). Then, the helicity shift is refined in the structures of fibril filaments, which are specialized for the shift without change in length, and travels down along the ribbon and cell axes, based on the axial cooperativity of the ribbon (13). The idea that the helicity shift is caused by coordinated changes in filament lengths is common with a previously suggested model, although they assumed that fibril filaments aligned at outer zones change their lengths actively (17). The dumbbell may have a role in triggering the helicity shift because the shift starts from the front (Figure 4B). The kink sometimes

reverses the traveling direction to achieve chemotaxis, suggesting that cooperativity is not completely directed (19). Note that this working model is still an early version and will hopefully be refined by additional findings in the near future.

Evolutional origin of swimming mechanism

MreB, the ancestor of SMreB, plays the role of assigning “elongasome,” the complex for PG synthesis to appropriate positions, by detecting the cell membrane curvature (25). Although MreB belongs to the actin superfamily, it is currently not thought to control cell morphology through its filament structure. Therefore, the roles suggested for SMreBs appear far from those of conventional MreBs. The five classes of SMreB isoforms form a group at a position phylogenetically distant from the conventional MreB and closer to MreBH (14, 26, 27). Each SMreB isoform is suggested to have different characteristics regarding ATP hydrolysis, filament formation, membrane binding, and interaction with other proteins (14, 26, 28, 36, 39). It is possible that in the course of their evolution, the early stage of SMreBs separated into classes to obtain the bi-metallic strip dynamics, which was suggested in Fig. 4. *Haloplasma contractile*, belonging to class Mollicutes, is more related to the phylum Firmicutes than *Spiroplasma* is (40). *H. contractile* cells have seven MreBs but no fibrils, whereas *Spiroplasma* has a single fibril protein (26, 27). Interestingly, *H. contractile* switches between stretched straight and corkscrew-like contracted shapes. This suggests that *H. contractile* contracts by a mechanism related to the early version of *Spiroplasma* swimming (40).

The N-terminal domain of the fibril protein has approximately 20% amino acid sequence identity with an SAH nucleosidase, an enzyme that hydrolyzes S-adenosyl-L-homocysteine (Figure 5A). This protein is essential for bacterial growth because it recycles adenine and methionine by digesting methylthioadenosine (MTA) and S-adenosylhomocysteine (SAH), and also produces a quorum-sensing signal, autoinducer-2 (AI-2) (41). SAH nucleosidase is widespread in bacteria and is known to be a target for antibiotics. SAH nucleosidase forms a dimer by facing its N-terminal regions and undergoes conformational changes at the intra- and inter-subunit levels in the hydrolyzing reaction of the glycosyl bond (Figure 5B) (42, 43). The structural changes in the fibril protein during swimming may originate from these conformational changes. Fibril protein showed conservation levels as high as 51%, with completely identical amino acids in all 22 *Spiroplasma* species (Figure 5A). This number is much higher than that of SAH nucleosidase, 10% in the 22 species, indicating

that any mutations of fibril protein are unacceptable in most amino acids if fibril protein was not distributed through horizontal transfer.

Perspective

Motility is thought to originate from the occasional transmission of large movements inside the cell, including DNA maintenance, ATP synthesis, and material transportation to the outside environment across the cell membrane (5). However, this hypothesis has not been validated because few proteins involved in motility systems can be traced back to their ancestors. They were most likely refined rapidly during selection for efficient locomotion in their development. Swimming motility in *Spiroplasma* can be traced for its evolutionary origin, suggesting that the class Mollicutes is a young group of bacteria. If we trace this evolutionary process experimentally at the atomic level, it would provide a clue to clarify the principle underlying the evolution of both cell and motility.

Funding

This study was supported by the Grants-in-Aid for Scientific Research A (MEXT KAKENHI, Grant Number JP17H01544), JST CREST (Grant Number JPMJCR19S5), and the Osaka City University (OCU) Strategic Research Grant 2017 for top priority research to MM.

Acknowledgments

I thank Pananghat Gayathri at the Indian Institute of Science Education and Research, Pune, India for the images in Figure 4, as well as Hana Kiyama, and Ikuko Fujiwara at the Graduate School of Science, Osaka City University, Japan for helpful discussion.

Figure and legends

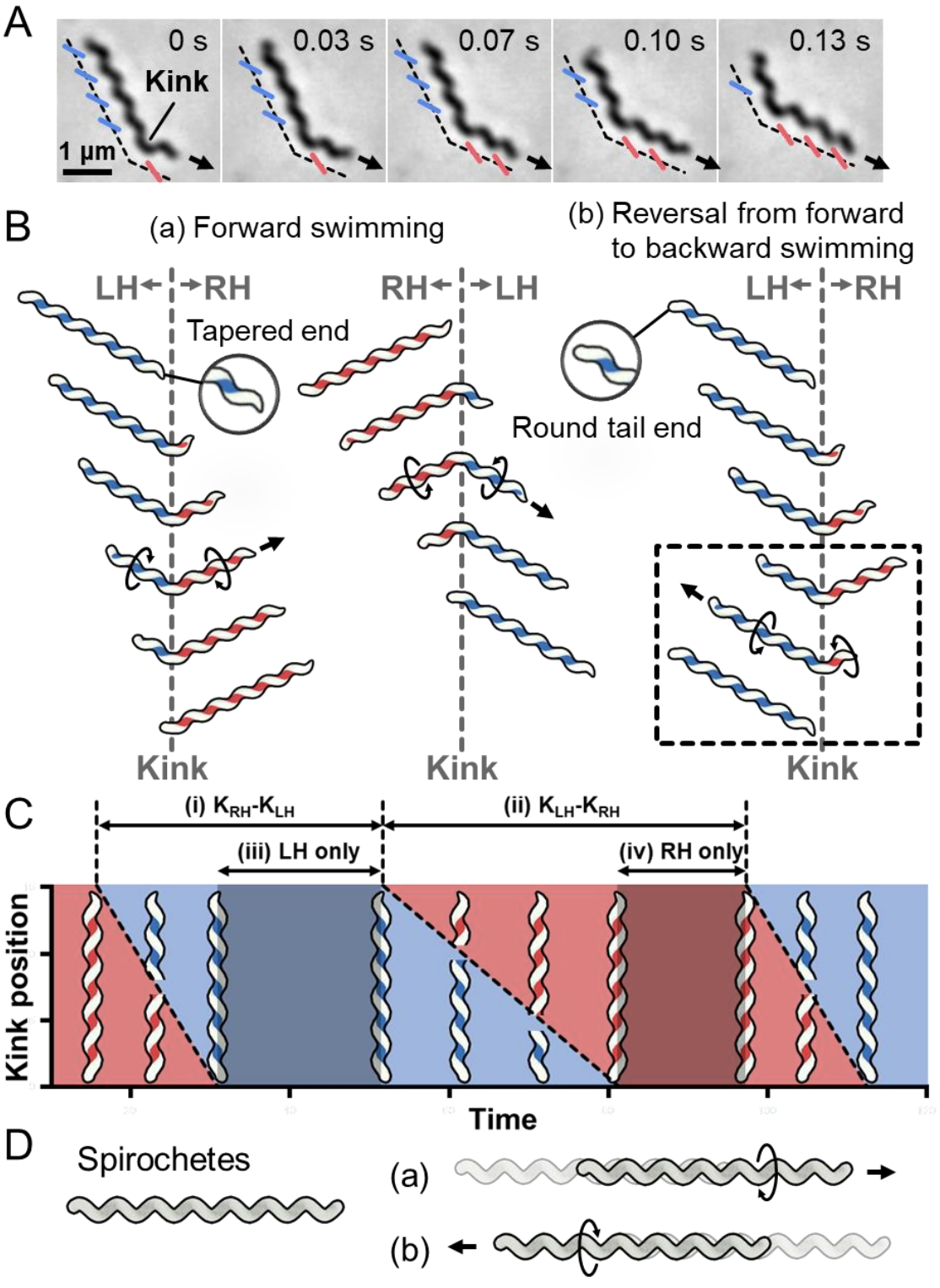

Figure 1. Helicity-switching swimming of *Spiroplasma*. (A) Phase-contrast microscopy of swimming cell. The blue and red lines indicate the left and right

handedness (LH and RH) of the helical cell morphology, respectively. The swimming direction is indicated by the arrow. Time is shown in seconds at the upper right of each panel. (B) Swimming schematics. A kink is formed at the boundary of the different handedness. Counter-rotational torque is generated backward and forward of the kink position as shown by circular arrows. (a) The cell basically swims in the direction of the tapered end. (b) Sometimes cells reverse the direction of kink traveling, resulting in swimming reversal. The reversal kink traveling is presented in the dashed box. (C) Schematic diagram of kink position as it travels along the whole cell length during swimming. The time when the cell helix keeps LH and RH is colored blue and red, respectively. The intervals of the kink productions are indicated by (i) and (ii). The time when the cell keeps the body as LH and RH is marked as (iii) and (iv), respectively. This is a schematic presentation of previous data (13). (D) Schematic for Spirochetes swimming. The helical cell has the same handedness throughout the whole cell length. The cell swims forward by rotating the cell helix in one direction (a), or backward after switching the rotational direction (b).

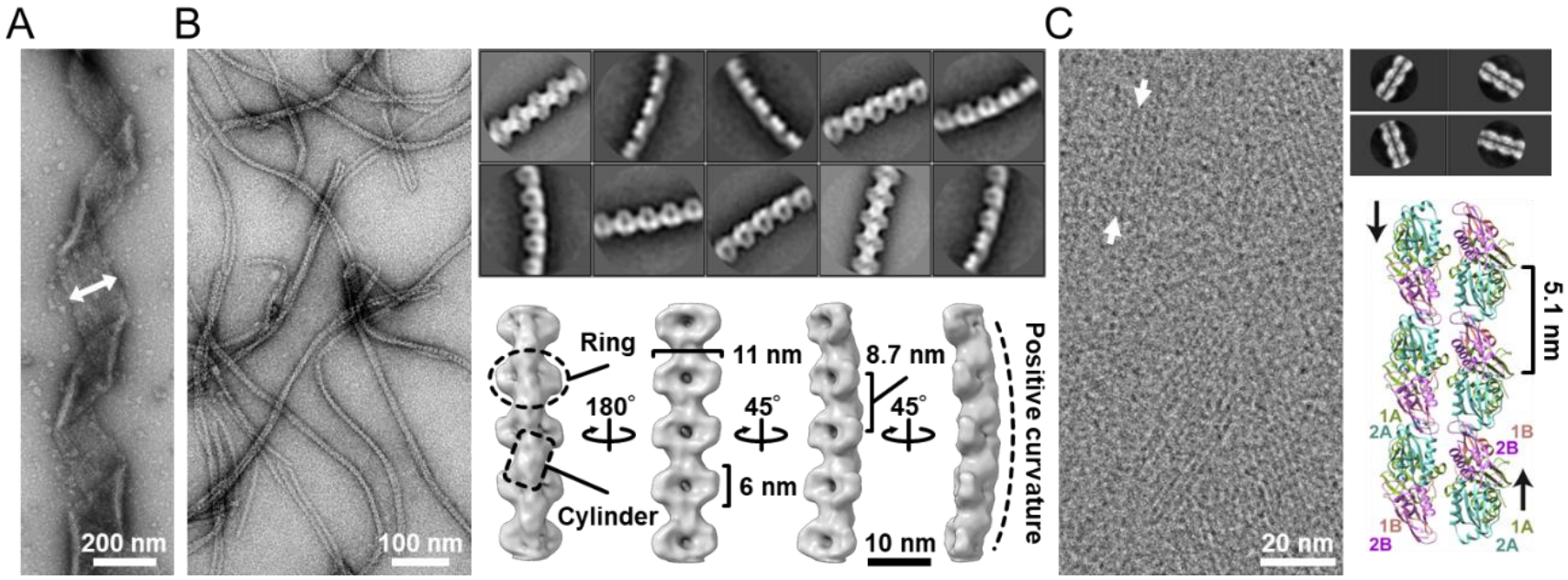

Figure 2. Ribbon components. (A) Negative staining electron microscopy of ribbon. The ribbon width is 150 nm long and is indicated by the two-headed arrow. (B) Structure of fibril filament. Negative staining EM of the isolated fibril filament (left). 2D class averages derived from the electron micrographs of fibril filaments (right upper). The three-dimensional structure of the fibril filament (right lower). A ring and a cylinder are marked by an oval and a box, respectively. The filament has 8.7 nm periodicity along the axis and positive curvature as marked by a broken line. (C) Cryo-EM image of *Spiroplasma citri* SMreB5 filament (left). Averaged image of the double stranded MreB filament (right upper). A model of double protofilament of *S. citri* MreB5 generated by superposing structure of *S. citri* SMreB5 (PDB ID: 7BVY) on *Caulobacter crescentus* MreB (4CZE). This panel was reorganized from a previous article (14) under permission.

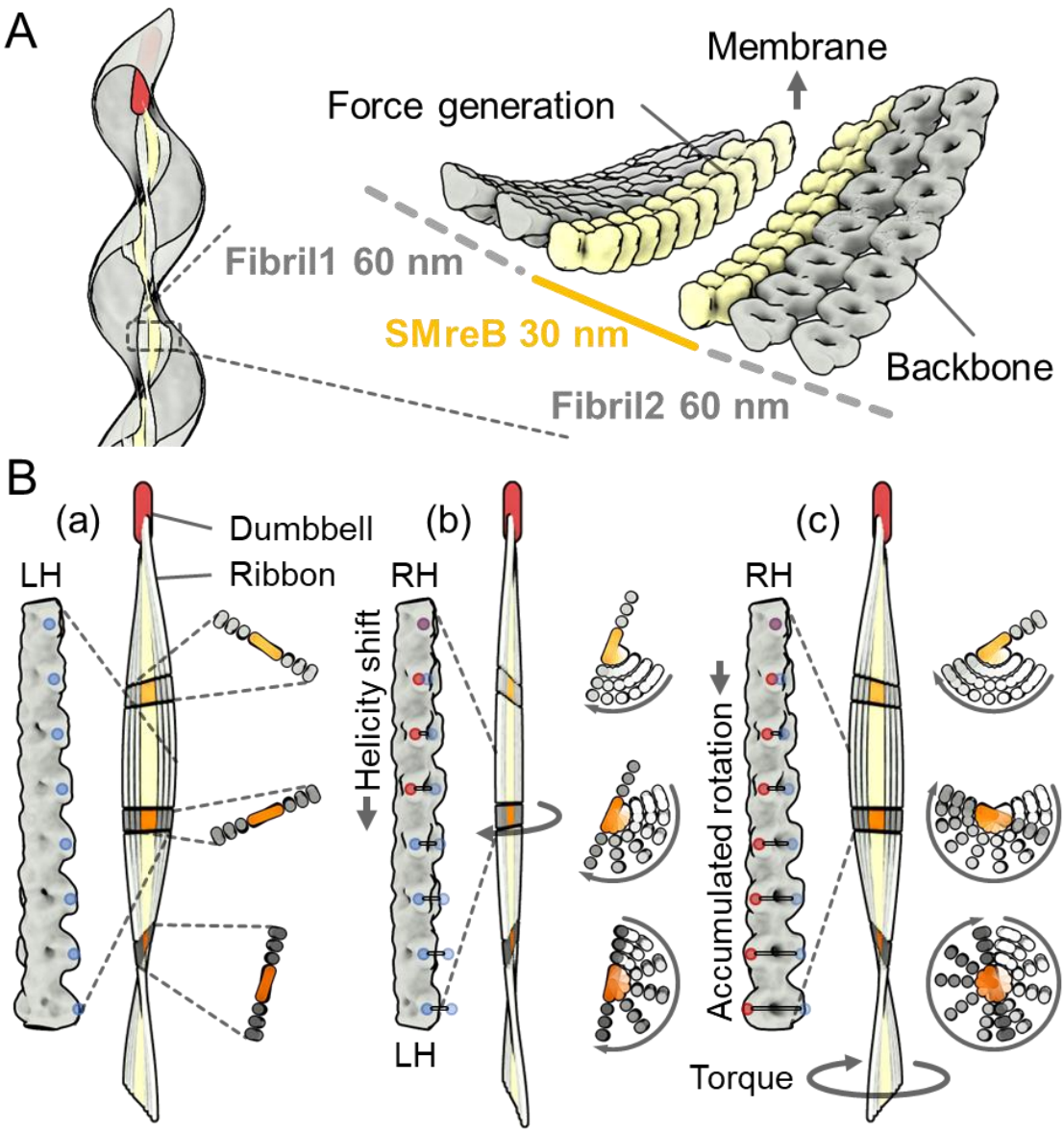

Figure 3. A working model for the helicity shift showing the propulsion of the cell body by pushing the water backward. (A) Left: Ribbon alignment along the innermost line of the helical cell body. Right: A model for ribbon composed of SMreB and fibril filaments, suggested from cryo-EM (17). The fibril protein is aligned in outer zones that are each 60 nm wide. SMreB molecules are aligned in the inner zone which is 30 nm wide. (B) Ribbon rotation caused by accumulated twists. An LH ribbon (a), a transition state from LH to RH (b), and the resulting RH ribbon (c) are presented. The magnified image of the fibril filament in the ribbon, the whole ribbon, and the small stack of the ribbon are shown on left, center, and right panels, respectively, for the three conformations (a), (b) and (c). The ribbon is fixed at the cell front by a dumbbell structure. The rotation of the

small stack from the conformation (a) is shown by traces with different transparency in (b) and (c). The twists of the fibril filaments accumulate with the ribbon rotation. The accumulated twists push the water backward and generate a propulsion force. LH and RH points are marked by blue and red dots, respectively. The traces of the colored dots from the original positions in (a) are shown as horizontal lines in (b) and (c).

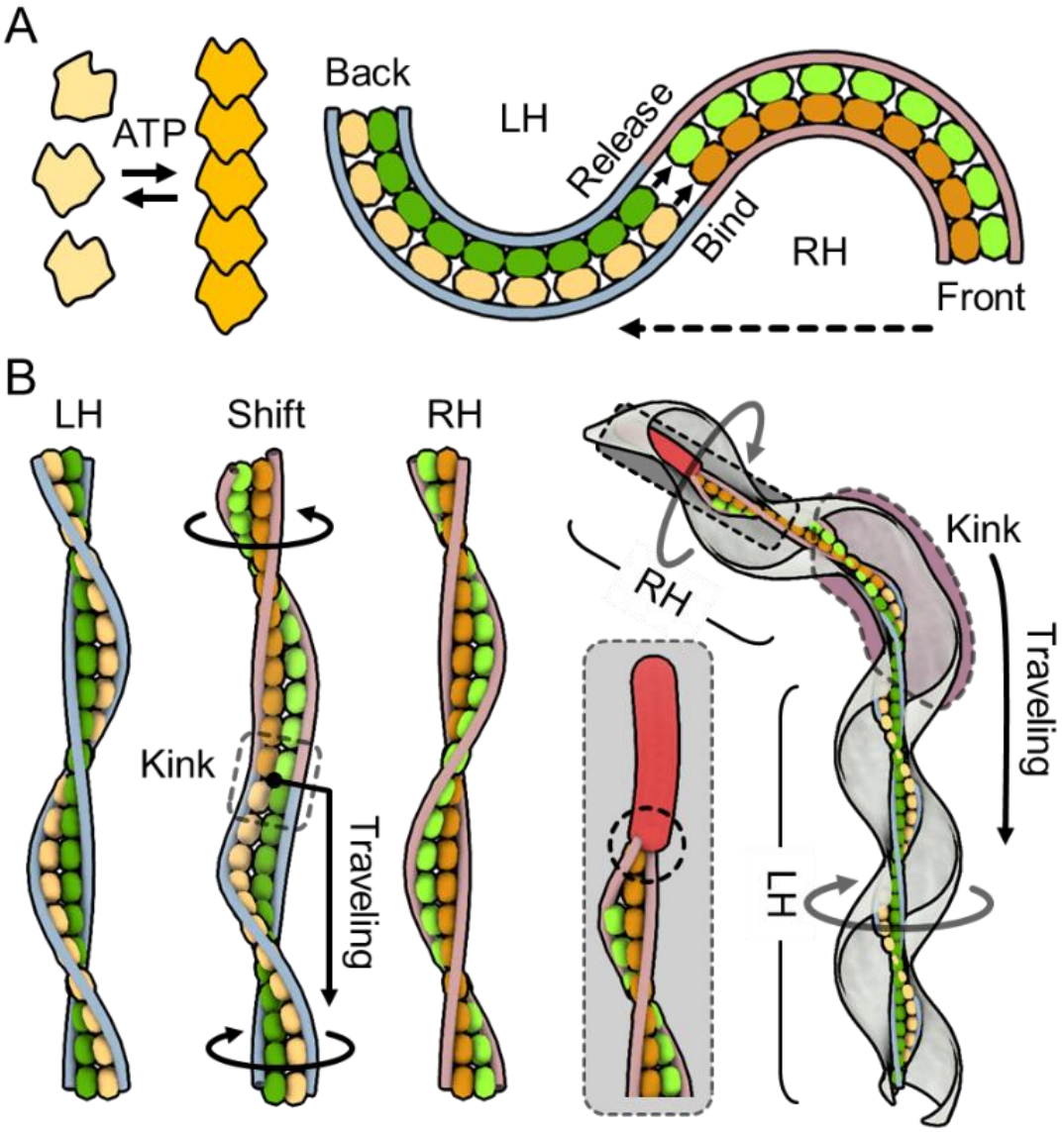

Figure 4. One working model for force generation and the transmission mechanism. SMreBs are presented as free and chained molecules. Two classes of SMreBs are colored yellow (light or dark) and green (light or dark). Fibril filaments are shown as blue (LH) and red (RH) strings without detailed structures for simplicity. Monomeric, polymerized, dissociated, and associated SMreB molecules are colored light yellow, dark yellow, light yellow or green, and dark yellow or green, respectively. (A) Bi-metallic strip action of the ribbon suggested from characters of SMreB and fibril filaments. Left: Polymerization based on ATP energy is observed in some MreBs. Right: Helicity shift caused by length changes occurring differently in individual SMreB filaments. Left-handed (LH) ribbon shifts to right-handed (RH) from the front as shown by the broken arrow. The length changes in SMreB filaments related to polymerization dynamics of

MreBs cause the helicity shift. Here, contraction is simply coupled to the association of molecules, but many other scenarios can be considered. (B) Three-dimensional presentation for helicity shift originated from bi-metallic strip action of SMreB filaments. For simplicity, the ribbon is presented by the central paired SMreB filaments and the peripheral two fibril filaments. Left: LH, shifting (Shift), and RH ribbons are shown. In shifting, the yellow SMreB filament is switching from extended to contracted states, and the green filament is switching in the opposite way. Helicity shift propagates from upper to lower regions. A kink observed around the shifting point travels along the ribbon axis as shown by the black arrow, through the cooperativity of the structural changes. The upper and lower parts of the ribbon rotate relative to the switching point as indicated by black circular arrows. Right: Schematic presentation of a swimming cell. The dumbbell fixes filament movements at an end as marked by a broken circle, giving directionality to the ribbon. The kink travels down along the entire cell axis as shown by the black arrow, generating the counter-rotational torques in the front and back position of the kink. It also sometimes changes its traveling direction, showing the reversibility of the conformational changes.

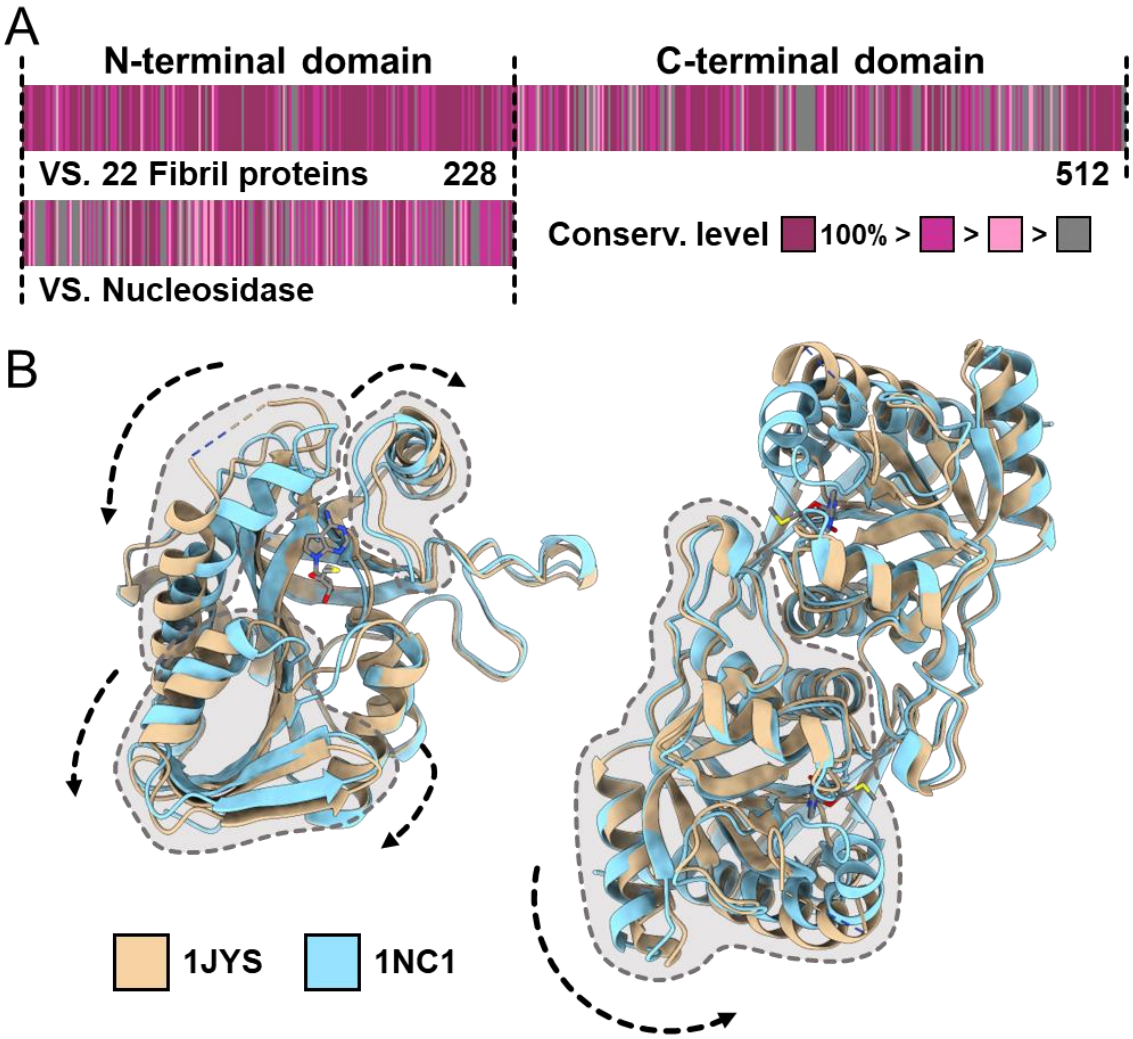

Figure 5. Evolutional origin of fibril protein. (A) Amino acid sequence of *Spiroplasma eriocheiris* fibril protein. The fibril protein, comprising of 512 amino acids can be divided into the N-terminal domain including 1-228 amino acids, which has homology to bacterial SAH nucleosidase, and the remained fibril specific C-terminal domain. The conservation level of the amino acid sequence among the fibril proteins from 23 *Spiroplasma* species (upper), and that against SAH nucleosidase from *Bacillus anthracis* (WP_098760943.1) are colored from gray (low) to purple (high) based on the Gonnet PAM 250 matrix (44, 45). (B) Conformational changes in SAH nucleosidase. The two structures of SAH nucleosidase from *Escherichia coli* (PDB ID: 1JYS, 1NC1) are superposed. The conformational changes intra- (left) and inter-subunit (right) are indicated by dashed arrows.

CHAPTER II

Isolation and structure of the fibril protein, a major component of the internal ribbon for *Spiroplasma* swimming

Keywords: Helical shape, Motility, Cytoskeleton, Filament, Single particle analysis, Quick freeze replica electron microscopy, Electron tomography.

Abstract

Spiroplasma, which are known pathogens and commensals of arthropods and plants, are helical-shaped bacteria that lack a peptidoglycan layer. *Spiroplasma* swim by alternating between left- and right-handed helicity. Of note, this system is not related to flagellar motility, which is widespread in bacteria. A helical ribbon running along the inner side of the helical cell should be responsible for cell helicity and comprises the bacterial actin homolog, MreB, and a protein specific to *Spiroplasma*, fibril. Here, I isolated the ribbon and its major component, fibril filament, for electron microscopy (EM) analysis. Single-particle analysis of the fibril filaments using the negative-staining EM revealed a three-dimensional chain structure composed of rings with a size of 11 nm wide and 6 nm long, connected by a backbone cylinder with an 8.7 nm interval with a twist along the filament axis. This structure was verified through EM tomography of quick-freeze deep-etch replica sample, with a focus on its handedness. The handedness and pitch of the helix for the isolated ribbon and fibril filament agreed with those of the cell in the resting state. Structures corresponding to the alternative state were not identified. These results suggest that the helical cell structure is supported by fibril filaments; however, the helical switch is caused by the force generated by the MreB proteins. The isolation and structural outline of the fibril filaments provide crucial information for an in-depth clarification of the unique swimming mechanism of *Spiroplasma*.

1 Introduction

Mollicutes, which are parasitic or commensal bacteria, evolved from the phylum, Firmicutes, including *Bacillus* and *Clostridium* by reducing their genome size (5, 8, 9, 46). During the course of evolution, the cells became softer and smaller owing to the loss of the peptidoglycan layer. These changes may have allowed some species to transmit the movements of their internal housekeeping proteins to the outside, resulting in the acquisition of at least three unique motility mechanisms (5, 11, 12, 47-50). Two of the three well studied mechanisms are exerted by *Mycoplasma mobile* and *Mycoplasma pneumoniae*. These species

exhibit gliding motilities on solid surfaces, in which leg structures repeatedly catch sialylated oligosaccharides on host cells based on two mechanisms (11, 12, 51). Another motility system is the helicity-switching swimming of *Spiroplasma*, which is the subject of the present study (Movie_S1) (1, 6, 7, 52). *Spiroplasma* species are parasitic to plants and arthropods and are characterized as polarized helical-shaped cells with one tapered end (1, 3, 53). These species exhibit obvious chemotaxis despite the absence of genes for the two-component regulatory system in the genome, which is generally responsible for bacterial chemotaxis (19). In general, swimming bacteria, including spirochetes, can migrate through the rotational motion of the flagellar motor fixed to the peptidoglycan layer, whereas *Spiroplasma* has a unique swimming system in which kinks propagate along the cell body with a switch between left- and right-handed cell helicity (Fig. 1A). The outline of this mechanism has been clarified as follows. The rotation of helical cells linked to the helicity switch pushes the water back (6, 7, 17, 52, 54, 55). The helicity might be dominated by an intracellular structure called the “ribbon,” which localizes along the innermost line of the helical cell structure and is composed of protofilaments. Based on structural studies, ribbons may switch their helicity through changes in the protofilament length (17, 24, 54). Ribbons are known to be composed of fibril proteins specific for *Spiroplasma* species and some *Spiroplasma* MreB (SMreB) proteins related to MreB that are common in rod-shaped bacteria. Although fibril filaments are featured by repetitive ring structures, nanometer-order three-dimensional structure has not been clarified (16, 17, 19, 24, 54, 56).

In the present study, I isolated the filament of fibrils, the major component protein of ribbons and clarified its nanometer-order three-dimensional structure using electron microscopy (EM) and image analyses. The fibril filament has a repetitive structure featuring a ring and a cylinder with a helical pitch similar to those of the ribbon and cell.

2 Materials and Methods

2.1 Bacterial strains and culture conditions

The type strain, TDA-040725-5^{T}, of *Spiroplasma eriocheiris* was cultured in R2 medium (2.5% [wt/vol] heart infusion broth, 8% sucrose, and 10% horse serum) at 30 °C until an optical density of 0.06 to 0.1 was achieved at 600 nm (19, 57).

2.2 Optical microscopy

Cultured cells were centrifuged at 11 000 × *g*, 10 °C for 10 min and suspended in PBS consisting of 75 mM sodium phosphate [pH 7.3], 100 mM NaCl containing 20 mM glucose, and 0.6% methylcellulose, to achieve a cell density 10-fold higher than that of the original (19, 57). Cells were inserted into a tunnel chamber

assembled by taping coverslips, as previously described, and observed under an IX71 microscope (Olympus, Tokyo, Japan) (58). A video was captured using a DMK33UX174 complementary metal–oxide–semiconductor (CMOS) camera (The Imaging Source, Taipei, Taiwan) and analyzed using ImageJ v1.53a (https://imagej.nih.gov/ij/).

2.3 Electron microscopy

To observe the intact cells, the cell suspension was placed on a hydrophilized grid, fixed using 2% glutaraldehyde, washed with water, and stained with 2% uranyl acetate. To observe the internal structure, the cell suspension on a grid was treated with PBS containing 0.1 mg/mL DNase and 1 mM $MgCl_2$ for 20 s, washed, and stained with 2% uranyl acetate. QFDE-EM was performed as previously reported for specimens suspended in a solution, 10 mM HEPES (pH 7.6), and 150 mM NaCl containing mica flakes (59). The Triton X-100 treatment was done on glass surface before freezing, to observe the internal structure. Images were acquired using a JEM1010 EM (JEOL, Akishima, Japan) equipped with a FastScan-F214(T) charge-coupled device (CCD) camera (TVIPS, Gauting, Germany) and analyzed using ImageJ v1.53a. For tomography, images were captured using a Talos F200C EM (FEI, Eindhoven, Netherlands) equipped with a 4k × 4 K Ceta CMOS camera (FEI). Single-axis tilt series were collected covering an angular range from -50° to +50° with 1.5° steps and analyzed using IMOD (ver 4.11) and PEET (ver 1.15.0).

2.4 Isolation of the ribbon and fibril

To isolate the internal structure, 10 mL of cell suspension in PBS was treated with 1% Triton X-100, 0.1 mg/mL DNase, 1 mM $MgCl_2$, and 0.1 mM PMSF, with shaking for 10 min at 4 °C. The insoluble fraction was recovered via centrifugation at 20 000 × *g* for 30 min at 4 °C, and suspended in PBS to obtain a final volume of 0.2 mL. The sample was placed at the top of sucrose solution layers of 0%, 20%, 30%, 40%, 50%, and 60%, and centrifuged at 20 000 × *g* for 20 min at 4 °C in a 1.5 mL tube at a fixed angle. To isolate the fibril filament, the insoluble fraction was additionally treated with a solution consisting of 2% cholic acid, 20 mM Tris-Cl pH 8.0, 150 mM NaCl at 4 °C for 8 h, and subjected to stepwise density gradient centrifugation. SDS-PAGE and peptide mass fingerprinting were performed as described previously (19, 60, 61). Band intensities were calculated using ImageJ, from scanned gel images.

2.5 Preparation of the single-stranded fibril filament

The isolated fibril was adjusted to 1 mg/mL in 20 mM Tris-Cl pH 8.0 and 150 mM NaCl. The fibril suspension (1 mL in a 1.5 mL test tube) was treated on ice for 5 s

using a sonicator (UR-21P, TOMY, Tokyo, Japan). The condition of the fibril filament was checked via negative-staining electron microscopy (EM). The processes of sonication and observation were repeated with the fibril suspension until more than 90% of the filaments became single-stranded.

2.6 Reconstitution of the 3D structure

The contrast transfer function (CTF) parameters for negative-staining EM images were estimated using the Gctf25 software (62). The images of fibril filaments were selected automatically using RELION 3.0 (63) as helical objects and segmented as squares of 200 × 200 pixels with a 90% overlap. These 14,543 images were 2D-classified and 11,867 images were selected for further analyses. *Ab-initio* reconstitution was performed using cisTEM (64) based on segmented images from 12 classes. The selected 11,867 particle images were 3D-classified using the 3D map in RELION 3.0 (63).

3 Results

3.1 Cell helicity is derived from the internal ribbon structure

To clarify the relationship between the helical cell morphology and the internal ribbon structure, I first measured the helical pitches of the swimming cells using optical microscopy. Under phase-contrast microscopy, the helical shape of the cells can be observed as a series of dense segments in the defocused image plane relative to the cell axis (Fig. 1A). I measured the pitches along the cell axis for the segments of left and right handedness (Fig. 1F). The helical pitches were 709 ± 74 (n = 50) and 718 ± 65 nm (n = 50) for the left- and right-handed segments, respectively.

EM was subsequently employed to analyze the internal ribbon structure and compare the helical pitches of the cells and ribbons. Negative-staining EM revealed images of helical-shaped cells with a narrow tip on one side (Fig. 1B).

The internal ribbon structure was exposed by treating the cells with 0.1% Triton X-100 on the grid (Fig. 1C). The ribbon had a “helical” flat structure. These observations are consistent with those of previous studies (54). Thereafter, the pitches of the cell and the exposed ribbon were measured (Fig. 1F). Generally, the specimens for negative-staining EM are placed in vacuum and dried, which can result in distortions and is disadvantageous for evaluating the helicity. I therefore applied quick-freeze, deep-etch (QFDE) EM to visualize the structure in a state as closely as possible to the original (65). In QFDE, a sample is frozen in milliseconds and exposed by fracturing and etching. Thereafter, a platinum replica was created by shadowing. The observation of the replica by transmission EM provides images with high contrast and resolution, which is markedly better than that provided by conventional scanning electron microscopy (SEM) (59, 65).

Replicas were then prepared by fracturing and platinum coating. QFDE-EM revealed cell morphology consistent with that obtained using negative-staining EM (Fig. 1D). Using QFDE-EM, I observed the ribbons exposed to 0.1% Triton X-100 treatment (Fig. 1E). The ribbon had a structure in which the twisted positions were assembled in a line, showing that the images observed by negative-staining EM were flattened. Interestingly, all ribbons were left-handed (Fig. 1D, E). When the cells were starved in phosphate-buffered saline (PBS) without glucose for 30 min, they showed a left-handed helix with the same pitch. Therefore, this structure was assumed to be the default state of the cell, and the ribbon switched to the default structure during the visualization process. The helical pitches of the cells and ribbons aligned well with each other, indicating that the ribbon has a critical role for cell helicity (Fig. 1F, Table 1).

3.2 Isolation and characterization of the ribbon

For further characterization, I isolated the internal ribbon structure. The cell suspension was treated with 1% Triton X-100 and subjected to stepwise gradient centrifugation with 0%, 20%, 30%, 40%, 50%, and 60% sucrose layers. After centrifugation, I found a dense layer of cell contents at the bottom of the 40% sucrose layer. The fraction was recovered and then observed by EM. Based on the observation, the ribbon was found to comprise protofilaments with a width of 66 ± 12 nm (n=20) and a length longer than 2 μm, which may correspond to the full length of the cell (Fig. 2A). To analyze the number and width of the protofilaments involved in the isolated ribbon, I traced a cross sectional image profile of the ribbon (Fig. 2D a). Six to nine protofilaments were detected, with peak distances ranging between 4 and 16 nm (Fig. 2D b, c), consistent with the findings of the previous studies (19, 54). Ribbon twists are observed as periodic frays in the ribbons. The ribbon pitches were measured from the frays as 350 ± 17 nm (n = 47) (Fig. 2D d), which is comparable to the helical pitches of the cells and the ribbons exposed from cells on grids (Fig. 1, Table 1) ($P = 0.7 > 0.01$). SDS-PAGE and peptide mass fingerprinting analyses of this fraction revealed five protein bands, including six proteins (Fig. 2B, Table 2, Table S1). Band (v) contains SMreBs 2 and 4. The whole ribbon fraction mainly comprised the fibril protein (band iii) and a protein mixture of SMreBs 2 and 4 (band v), with an intensity ratio of 47% and 37% of the total protein amount, respectively. Further studies are necessary to conclude physical interactions of SPE-1201 and FtsH to fibril protein, because these proteins are abundant in *S eriocheiris* cells (19).

I intended to use A22, an inhibitor of MreB polymerization, to examine the role of SMreBs in ribbon formation (25); this is because the binding of A22 to SMreBs has been suggested from amino acid sequences (26). First, the effect of 1 mM A22 on the swimming *Spiroplasma* cells was determined. The cells lost

their original shape and stopped moving within 2 min (Fig. 2C), suggesting that the functions of SMreBs were inhibited by A22. Thereafter, I isolated the ribbon from cells maintained in 1 mM A22 for 2.5 h at 30 °C. The ribbons were found to be dispersed (Fig. 2A, c). SDS-PAGE analysis revealed contents of 67% and 11% for fibril (band iii) and SMreB2 (band v) proteins, respectively (Fig. 2B), suggesting that the protofilaments comprising fibril proteins are stabilized and modified by SMreBs in the ribbon structure.

3.3 Isolation and helical pitch of the fibril filament

To analyze the detailed structure of fibril filaments, I treated the ribbon fraction with cholic acid and isolated fibril proteins using sucrose-gradient centrifugation. SDS-PAGE analysis showed that the fraction only contained fibril protein (Fig. 3A). Negative-staining EM revealed that the fibril protein formed filaments that included single-, double-, and more-stranded filaments, suggesting various types of interactions between the fibril protein molecules (Fig. 3B a). A single-stranded fibril filament consisted of repeated ring units with approximately 9 nm intervals (Fig. 3B b c), consistent with previous studies (19, 23, 54, 66). The ring units were connected by the backbone cylinder (Fig. 3B c). The double-stranded fibril filament appeared to be formed via the alignment of two single-stranded filaments contacting with each other at the ring side not the cylinder side, resulting in a thickness of 14 nm, double that of the single-stranded filament (7 nm) (Fig. 3B d e). I analyzed the helical pitches for the double-stranded fibril filaments as the double-stranded fibril filament had a sufficient length of stable helix to cover the pitch, with a clear twist of the ring pattern along the filament axis. Images of the fibril filament cropped from the electron micrographs using the straightening selection tool of the ImageJ software were subjected to Fourier filtering to remove noise (Fig. 3C). However, the handedness of the fibril filament could not be concluded as the negative-staining EM images are projections of the object, and the alignment of the filament on the EM grid was not distinguishable. Therefore, I analyzed the isolated fibril filament using QFDE-EM (Fig. 3D) as the replica synthesized with platinum covers only one side of the object surface. The structures shared features with those from the negative-staining EM (Fig. 3D, Fig. S1). I succeeded in determining their handedness (Fig. 3D a–f) and concluded that the double-stranded fibril filament formed a left-handed helix. The half pitch was distributed at 351 ± 33 nm (n = 50), which aligns with the results of negative-staining EM (Fig. 3E). The agreement of helix pitches in the cell, isolated ribbon, and fibril filament suggests that the fibril filament is a major component of ribbon formation and cell helicity (Table 1).

3.4 Three-dimensional reconstruction of the fibril filaments

To clarify the fibril filament from a three-dimensional (3D) viewpoint, a single-particle analysis was performed on negative-staining EM images. The double-stranded fibril filament was not suitable for image averaging, which might be due to the positional variation in the binding of the two filaments (Fig. 3 and Fig. S2). Therefore, I sonicated the purified fibril fraction to increase the proportion of single-stranded filament and successfully acquired single-stranded images (Fig. 4A). From the selected 11,867 particles with good quality, the 2D-averaged images were classified into three types: (i), (ii), and (iii) (Fig. 4A b). The initial 3D image was reconstructed using the *ab-initio* 3D function of cisTEM software (64), and used as the reference for the subsequent 3D classification (Fig. 4A c). 3D structures of the fibril filament reconstructed from 11,867 particles using RELION 3.0 revealed three different conformations (i.e., class 1, left-handed mainly straight (49%); class 2, left-handed with curvature (24%); and class 3, right-handed with curvature (27%) (Fig. 4A d and Fig. S3). The class 1 structure reconstituted with rotational symmetry (C2) was not significantly different from that without symmetry (C1), suggesting that the fibril filament had rotational symmetry without polarity (Fig. S3). I therefore reconstructed the structures of the fibril filaments with C2 symmetry. The 2D reprojections from these three structures corresponded well with the 2D class averages, indicating the validity of the obtained 3D structures (Fig. S3). The 3D structure of the fibril filament had repeating elliptical rings with a pitch of 8.7 nm along the filament axis, and the ring size was 11 wide and 6 nm long along the filament. A short backbone cylinder tilted slightly to the right was found to connect the ring units, resulting in a positive curvature (Fig. 4A d). These characteristics were common to all three classes.

Although the superimposition of class 1 and others showed their structural diffferences, the positions responsible for the differences could not be identified owing to the low resolution of the structures (Fig. 4B). The fibril filaments of all classes were twisted along the filament axis, but with different rotational angles (Fig. S4). The twisting angles were estimated from the angle averages of the first and fourth units, as 5.9 (left-handed), 7.3 (left-handed), and 9.7 (right-handed) degrees for classes 1, 2, and 3, respectively. The twisting angles were estimated from the subunit numbers in the double-stranded images (Fig. 3) for negative-staining and QFDE-EM as 4.9 °and 4.7 °, respectively. These numbers slightly differed from those obtained from the reconstituted 3D structures, suggesting conformational differences between the curved and straight filament forms. These structures can explain the peak distance observed in the density profile of the isolated ribbon (Fig. 2D c, S5).

I proceeded to examine the variation in the ring interval (Fig. 4C, Fig. S6). 2D averaged images were measured for 60 ring intervals. The intervals were 8.86 ± 0.24 nm (n=60) and did not show group separation, suggesting that the intervals do not have clear conformational change, despite some having an elasticity up to 2.7%.

3.5 Handedness verified based on the tomography of the QFDE replica

The 3D images reconstituted from negative-staining EM had common features, despite variations in curvature and twist. The reconstructed structures all have rings and cylinders tilted slightly to the right along the filament axis when viewed from the front and back sides, respectively (Fig. 4A d), indicating that the three classes belong to the same side of mirror images. As the images by negative-staining EM are projections of the objects, the reconstituted structures may mirror images of the real structures. Thereafter, I intended to verify the handedness of the reconstituted structures by EM tomography of the QFDE replica sample (Fig. 5); this is because the tomogram cannot be a mirror image (67, 68).

I made QFDE replicas from the fraction containing single-stranded fibril filaments, acquired images every 1.5° to 50° specimen tilt for both directions, reconstituted tomograms (Movie_S4) (Fig. 5A), and then obtained a structure by averaging 60 subtomograms (Fig. 5B). As expected, the resulting filament structure had rings and cylinders. The rings and cylinders were tilted from the filament axis, rising to the right from the horizontal axis by 4–5 ° and 74–82 ° when viewed from the front and back, respectively (Fig. 5C and S7), which align well with the features of structures from negative-staining EM. These results indicate that the classes of structures from negative-staining EM had the same handedness as the real structures (Fig. 5C).

4 Discussion

4.1 Structures of the isolated fibril

The unique swimming of *Spiroplasma* is believed to be caused by the ribbon structure (1, 17, 24, 52). In this study, I isolated filaments of fibrils, the major protein of the ribbon, and revealed the 3D structure of the single-stranded filament at the nanometer scale using EM. Fibril filaments have been isolated for a long time, and their EM images show a characteristic ring repeat structure with a high contrast (19, 23, 24, 54, 56, 66). However, a nanometer-order three-dimensional fibril filament structure is yet to be revealed. Sonication during the isolation process was effective in isolating the single-stranded filament, whose uniform structure was advantageous for image averaging (Fig. 3). Negative-staining EM was used to reconstruct the structure (Fig. 4). However, as this method produces projection images, the handedness of the reconstructed

structure may be incorrect. Therefore, I confirmed the handedness of the structure by tomographic analysis of platinum replicas prepared by QFDE-EM (Fig. 5). The final structure was a repeating structure of elliptical rings connected by backbone cylinders aligned off-axis with a gentle left-handed helix, which is consistent with that of previous studies. No polarity was observed in the filament structure.

These results raise questions regarding the alignment of the 512 amino acid residues of the fibril protein with the structure and the structure formed by the 1-228 amino acid residues possessing obvious sequence similarity to methylthioadenosine/S-adenosylhomocysteine (MTA/SAH) nucleosidase (24, 41, 52). These questions will be answered via cryo-EM analysis of the single-stranded fibril filaments prepared in this study.

4.2 Ribbon structure in the cell

When *Spiroplasma* cells were lysed with a detergent, the ribbon structure appeared to run along the entire length of the cell axis (Fig. 1) (54). In this study, I isolated ribbons with a length equivalent with the entire length of the cell (Fig. 2). These observations suggest that the ribbon is a relatively stable structure rather than a highly dynamic one that disappears in a short time. Furthermore, as the extraction procedure with cholic acid yielded a structure consisting only of fibril filaments (Fig. 3), the stable properties of the ribbon are likely to be derived from the fibril filament. The helix of the fibril filament was directly observed in the double-stranded filament (Fig. 3). The constant helical pitch of a single strand could not be detected, which may be due to its irregular attachment to the EM grid. The two strands of double-stranded filaments may stabilize the inherent helical character of the filament by combining them. The handedness and pitch observed in the duplexes were left-handed and 351±34 (702±68) nm, respectively, aligning with the helical character of the cells at rest (Fig. 1, 3). As previous observations revealed the presence of ribbons in the innermost portion of the cell helix (16, 17), the helix of the resting cell should directly reflect the characteristics of the fibril filament.

During swimming, the cell switches its helical form into a right-handed one with a helical pitch similar to the left-handed one (Fig. 1). However, I could not find the corresponding right-handed helical structures in the isolated fibril filaments or ribbons. Only class 3 3D image reconstructed from 27% of the negative-staining EM images suggested a right-handed helical structure (Fig. 4); however, a further investigation is needed to conclude that this structure is stable one as the protein can be distorted by sticking to the EM grid in this analysis. These observations suggest that the right-handed helical structure observed in cells during swimming does not originate from another stable fibril filament

structure (Fig. 4). The helix switch can also be explained by assuming that two types of filaments running parallel to the ribbon are alternately extended and contracted (17, 24). To test this notion, I examined the distribution of the fibril filament lengths and found that the length distribution had a single peak at 8.86 ± 0.24 nm (Fig. 4). Such finding suggests that the fibril filament has only one stable length and does not support a helical switch caused by a length change in the fibril filament.

4.3 Role of fibril in the swimming mechanism

The fibril protein is conserved in most *Spiroplasma* species with high amino acid sequence similarity (27). However, *Spiroplasma sabaudiense* and *Spiroplasma helicoide* do not contain fibril proteins, despite exhibiting helicity-switching swimming (1). Recently, the expression of two SMreB proteins in the non-swimming synthetic bacterium, syn3.0B, was demonstrated to reproduce cell helicity and helicity-switching swimming (48, 69). Moreover, the expression of SMreB induced cell helicity and its switching in spherical Mollicutes species (70), implying that the helix formation of the cell and the force generation for switching are caused by SMreBs. Then, what is the role of fibril filaments in most *Spiroplasma* species? Isolated MreB binds to fibril filaments (14). Further, our results (Fig. 2) support the binding of SMreB to the fibril filaments. These observations suggest that MreB exerts a force on fibril filaments for swimming. SMreBs might cause helicity-switching swimming, and fibril filaments might be effective at obtaining high energy efficiency and chemotaxis; this is supported by the observation that swimming reconstructed in syn3.0B by SMreBs lacks processivity (48).

5 Funding

This study was supported by Grants-in-Aid for Scientific Research A (MEXT KAKENHI, Grant Number JP17H01544), JST CREST (Grant Number JPMJCR19S5), the Osaka City University (OCU) Strategic Research Grant 2017 for top priority research to MM, JSPS KAKENHI (Grant Number JP25000013), the Platform Project for Supporting Drug Discovery and Life Science Research (BINDS) from AMED (Grant Number JP19am0101117 and support number 1282), the Cyclic Innovation for Clinical Empowerment (CiCLE) from AMED (Grant Number JP17pc0101020), and JEOL YOKOGUSHI Research Alliance Laboratories of Osaka University to KN.

6 Acknowledgments

I thank Yuhei O Tahara, Daichi Takahashi, Hana Kiyama, and Ikuko Fujiwara at the Graduate School of Science, Osaka Metropolitan University, Japan, for their helpful discussions.

Table 1. Dimensions of the cell and ribbon

Parameters	Negative-staining EM	QFDE-EM	Optical microscopy
Cell helical pitch	706 ± 74 nm 703 nm	711 ± 41 nm (LH) 711 nm (LH)	709 ± 74 nm (LH) 702 nm (LH) 718 ± 65 nm (RH) 711 nm (RH)
Ribbon helical pitch	691 ± 53 nm 700 nm	700 ± 60 nm (LH) 706 nm (LH)	
Isolated ribbon 1/2 helical pitch	350 ± 17 nm 352 nm		
Isolated fibril 1/2 helical pitch	341 ± 27 nm 335 nm	351 ± 34 nm (LH) 352 nm (LH)	

Handedness is represented by LH and RH.

The upper and lower rows show the mean, standard deviation, and median, respectively.

Table 2. Protein components of the ribbon isolated from original cells[1].

Protein Band[1]	Gene ID	Annotation	Mascot Score[2]	Mass (kDa)[3]	Density ratio (%)	
					Original	A22 treated
(i)	SPE-1201	Hypothetical protein	72	85.8	4	5
(ii)	SPE-0013	FtsH	84	77.0	12	17
(iii)	SPE-0666	Fibril	206	58.7	47	67
(iv)	SPE-1231	SMreB5	98	38.5	10	7
(v)	SPE-1224	SMreB2	80	37.8	27	4
	SPE-1230	SMreB4		40.7		

[1] From A22-treated cells, the proteins common to the original cells were identified for bands (i)–(iv). For band (v) only, SMreB2 was identified.

[2] Mascot Score is the logarithm of probability that the observed match is a random event.

[3] Calculated from the amino acid sequence as a monoisotopic molecule.

Figure Legends

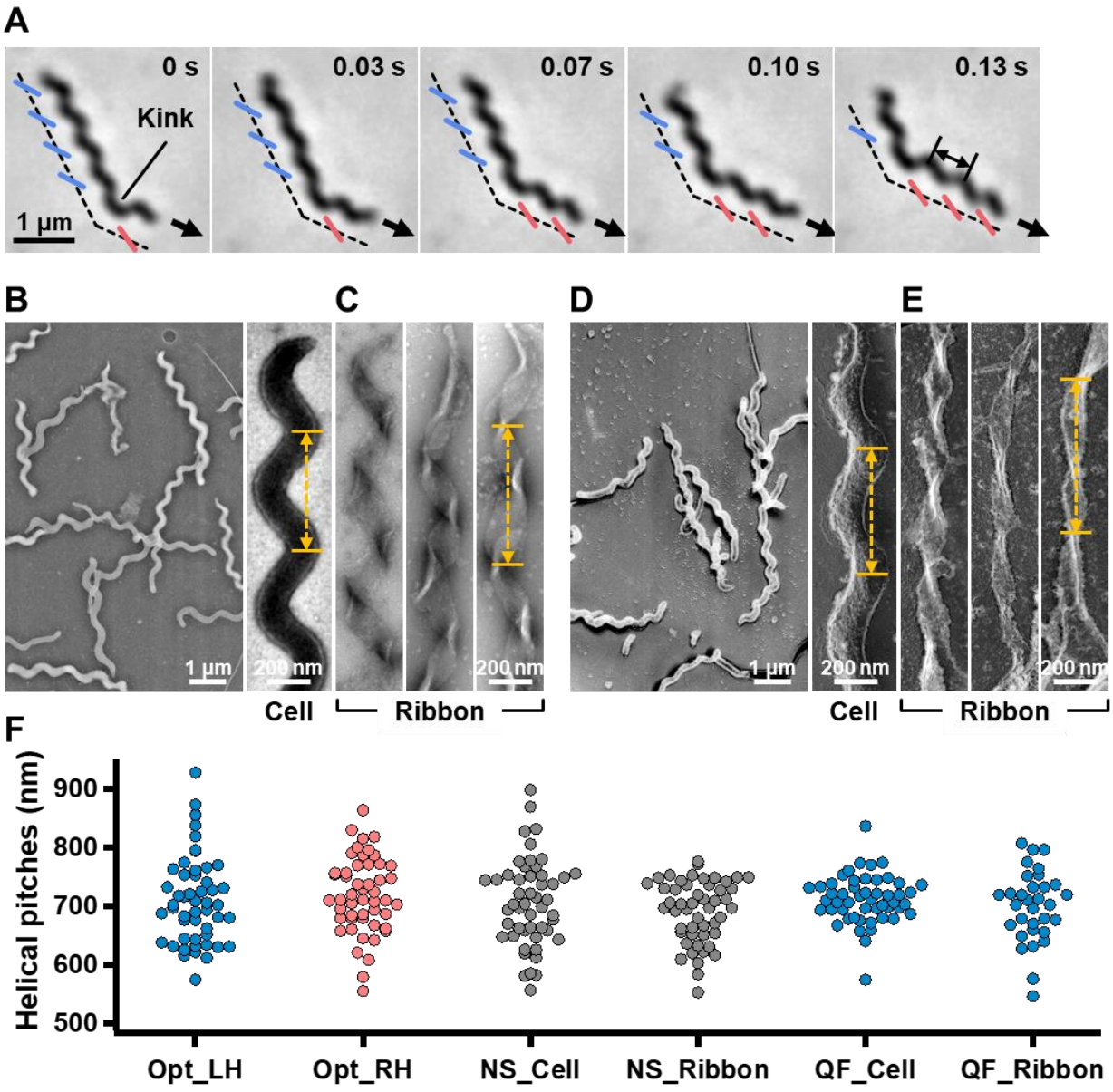

Figure 1. Helicity of the cell and ribbon structure. **(A)** Phase-contrast microscopy of swimming cell. The blue and red segments, and broken line indicate the left- and right-handed helicity, and cell axes, respectively. The pitch was measured as indicated by a double headed arrow. **(B, C)** Cell and ribbon images acquired by negative-staining EM. **(D, E)** Cell and ribbon images acquired by QFDE EM. (F) Helical pitches of cells and ribbon measured by optical microscopy, negative-staining EM, and QFDE-EM. Handedness was judged by optical microscopy and QFDE-EM. All cells analyzed by QFDE-EM were left-handed as they were grown under a starved condition.

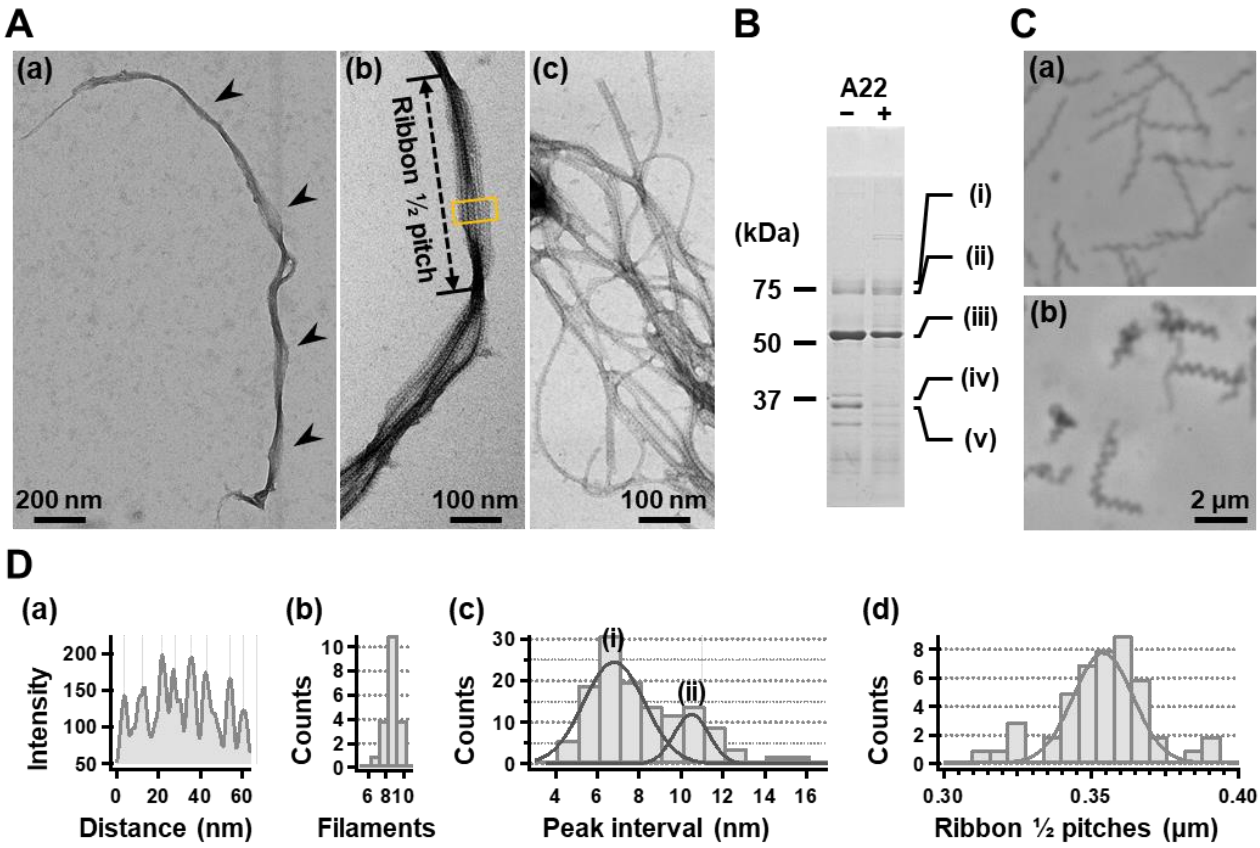

Figure 2. Isolation and characterization of the ribbon. **(A)** Isolated ribbon structure. (a) The whole structure of the isolated ribbon with helicity as shown by periodical wide positions (marked by arrows). (b) The magnified image of the isolated ribbon and the helical pitch is indicated by a bidirectional arrow. (c) Ribbon fraction isolated from cells treated with A22. **(B)** Protein profiles of the ribbon fraction isolated from cells untreated and treated with A22. **(C)** Cell images before (a) and after (b) treatment with 1 mM A22 for 2 min. **(D)** Numerical characterization. (a) Sectional image profile of the area boxed in panel (A b). The peaks correspond to the center of the protofilament. (b) Histogram for the number of protofilaments involved in a ribbon. (c) Histogram for the protofilament width in ribbons. The distribution can be fitted by two Gaussian curves marked (i) and (ii), with peaks around 7.0 and 10.5 nm, respectively. (d) Histogram for the helical pitches of the isolated ribbon, fitted by a Gaussian curve with a peak at 351 ± 16 nm (n=47).

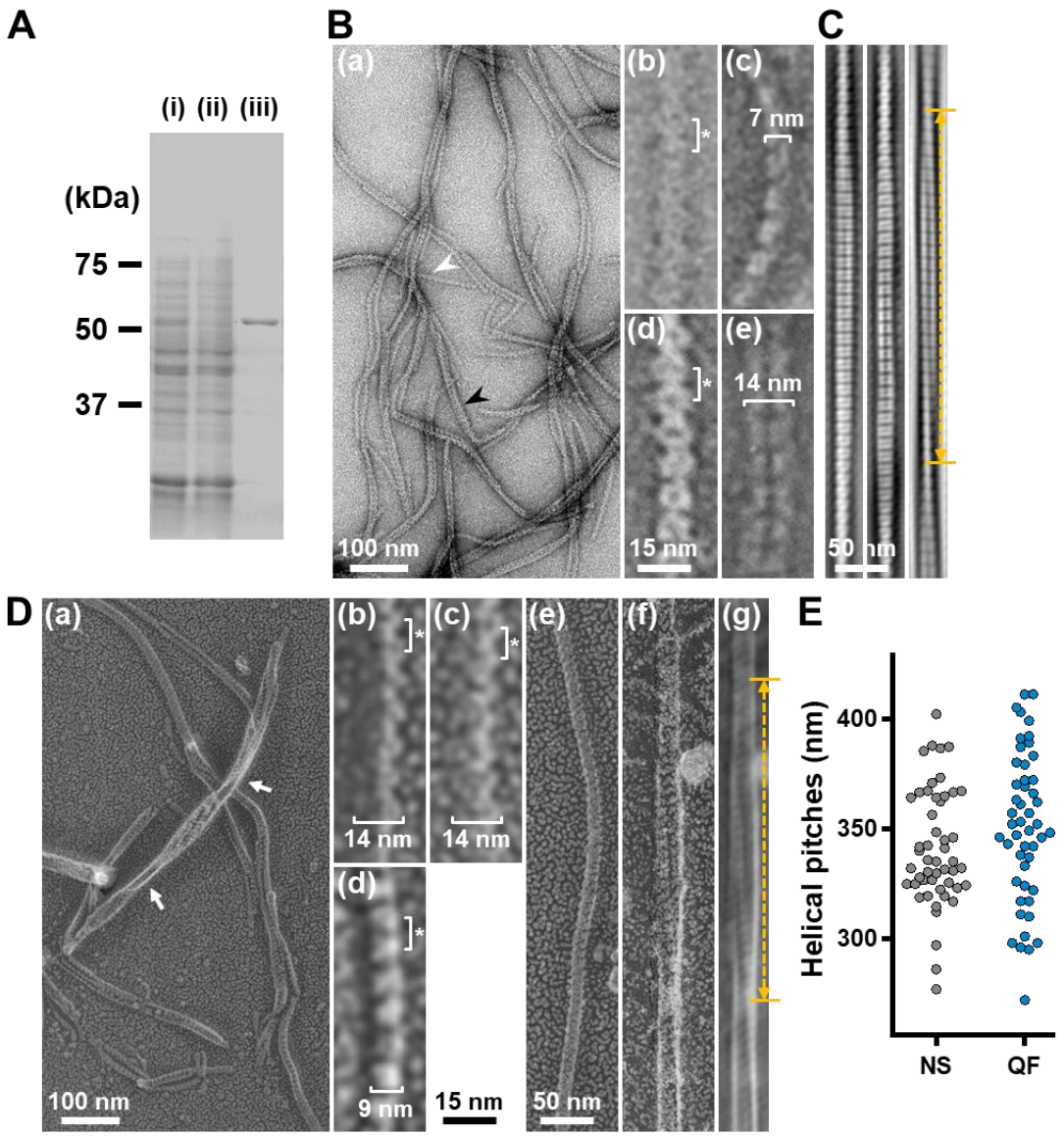

Figure 3. Structures of the isolated fibril filament. **(A)** Protein profiles of the fractions in the purification process for fibril protein. (i) Whole cell lysate. (ii) Supernatant. (iii) Isolated ribbon. The sample amount was adjusted to be delivered from the same cell number. **(B)** Purified fibril filaments observed by negative-staining EM. (a) Field image. White and black arrows indicate typical single and double strands, respectively. (b, c) Front and side views of the single-stranded fibril filament. (d, e) Front and side views of the double-stranded fibril filament. The ring intervals marked by an asterisk were 9 nm for both single and double strands. **(C)** Double-stranded filaments reconstituted through Fourier filtering. **(D)** Fibril filaments observed by QFDE-EM. Field (a) and single-stranded filaments (b, c, d) are presented. The back (b), front (c), and side (d) views are shown. (e) Single-stranded filament. (f, g) Double-stranded filament image (f) was reduced for noise through Fourier filtering. (g). The helical pitch was measured as depicted by a double headed broken arrow. The handedness was clearly observed at the points marked by white arrows in the panel (a) and panel (f) image.

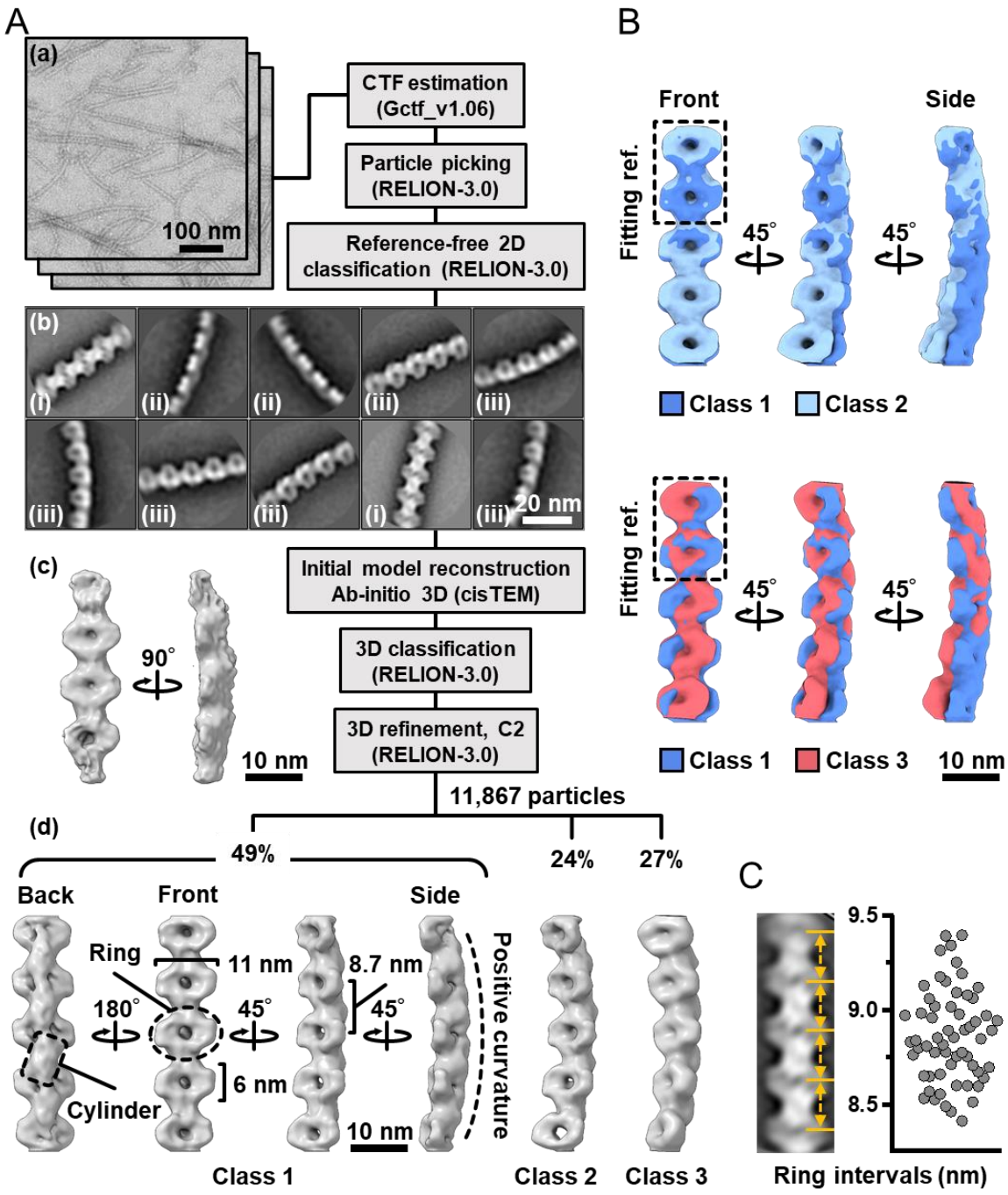

Figure 4. Three-dimensional reconstruction of the fibril filaments. **(A)** Workflow of single particle analysis by negative-staining EM. (a) Field images of single-stranded fibril filaments prepared by sonication. (b) Eight averaged images obtained by a function of 2D classification in RELION software. (c) The initial 3D model generated by a function of *ab-initio* reconstruction in cisTEM software. (d) Three different conformations of the fibril filament reconstituted by a function of 3D refinement in RELION software. **(B)** Superpose of class 1 (left-handed) and class 2 (left-handed) and 3 (right-handed) structures. The fitting reference is indicated by a dashed box. **(C)** Distribution of the ring intervals. Left: Ring intervals in an averaged image with complete rings. Right: Plotted ring intervals.

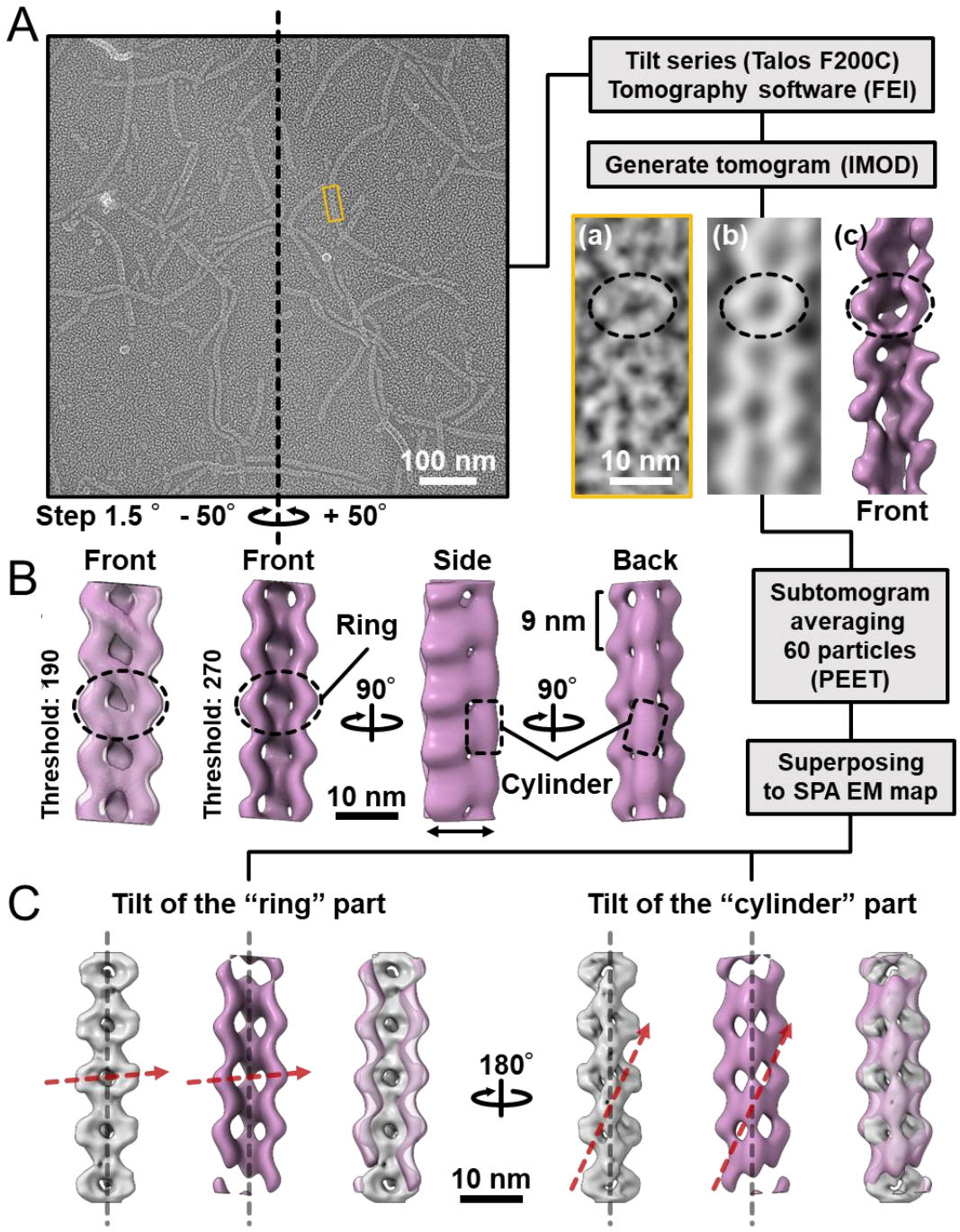

Figure 5. Comparison of the 3D structures of the fibril filament reconstructed from QFDE and negative-staining EM. **(A)** Replica image of mainly single-stranded fibril filaments. Left: A field image is shown from a tilt series (Movie_S2). Right lower: Magnified images of single fibril filament are shown as a raw image (a), a slice from the tomogram (b), and a subtomogram (c). **(B)** Structure averaged from 60 subtomograms. The leftmost image is presented under different thresholds from other three images. **(C)** Superpose of the 3D structures from single-particle analysis (grey) and subtomogram averaging (magenta). Long axes of ring and cylinder are depicted by broken red arrows. The filament axes were detected by a function "relion_align_symmetry --sym d2" in RELION-3.0.

Supplementary Material

1.1 Supplementary Figures

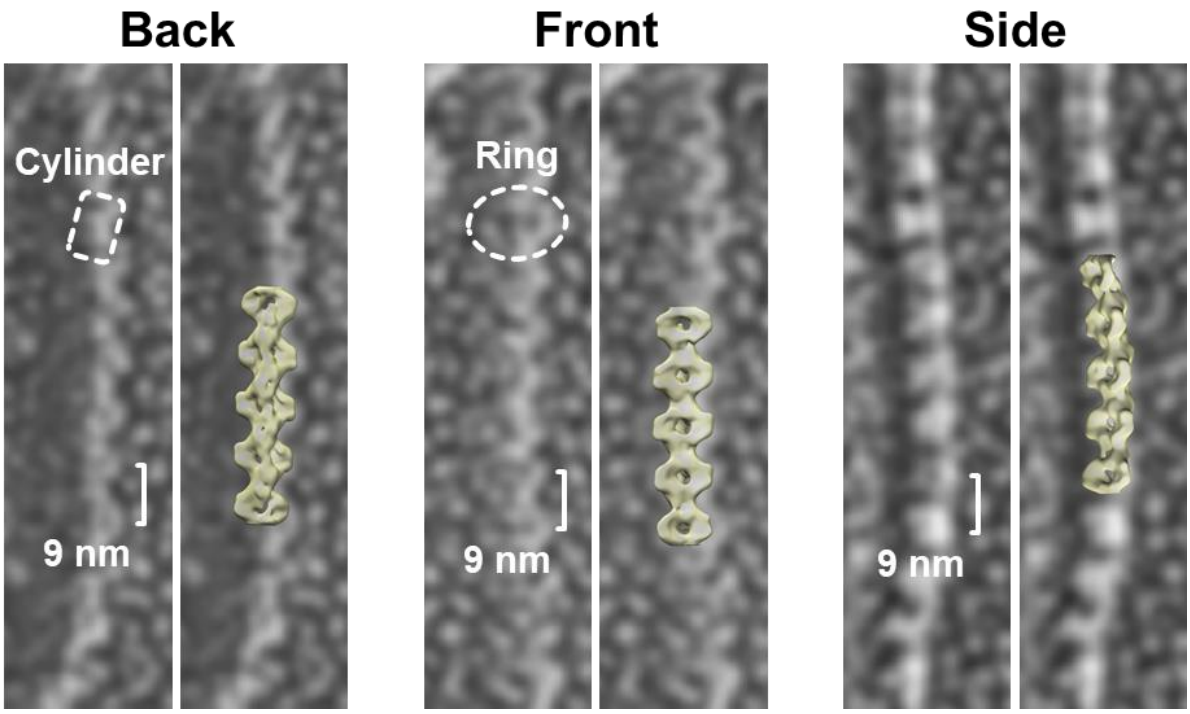

Supplementary Figure 1. Three alignments of the double-stranded fibril filaments were observed using QFDE-EM. The features and ring intervals of 9 nm are shown in the left image of each panel. Class 1 3D images reconstituted from negative-staining EM were overlaid on the right images.

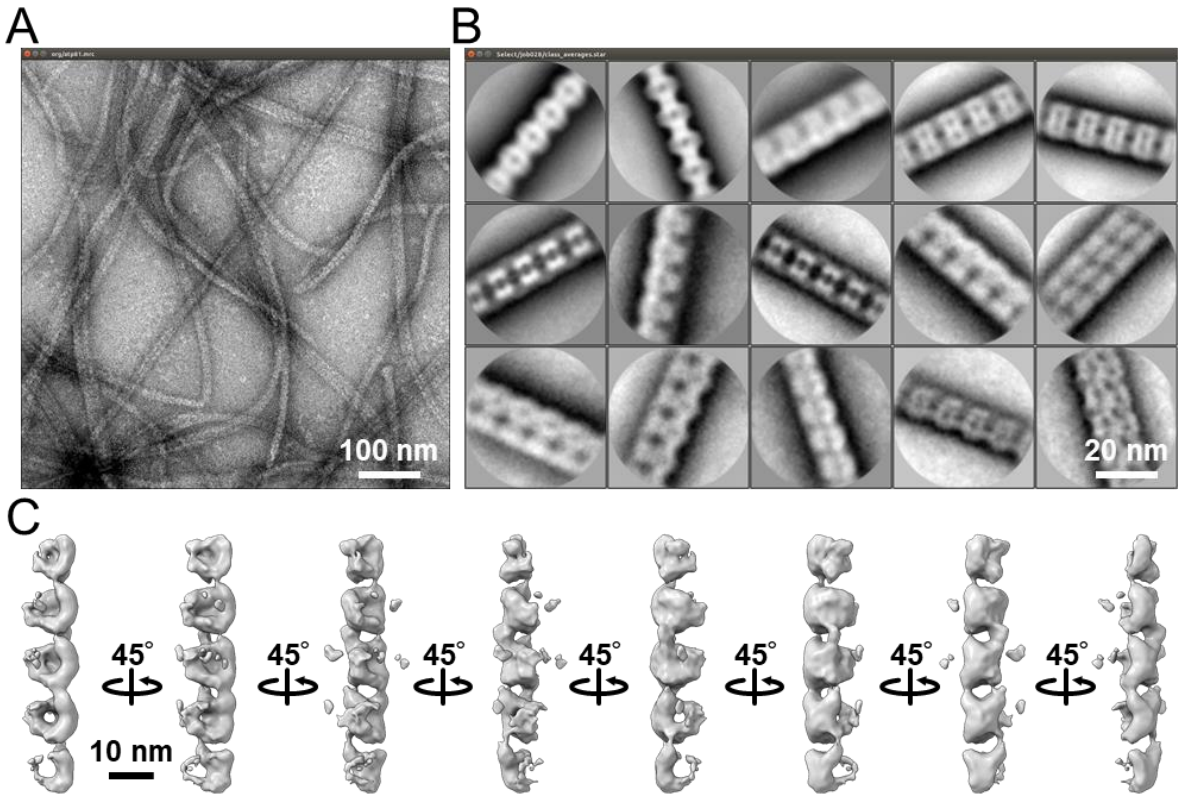

Supplementary Figure 2. Single particle analysis using double-stranded images. (A) Field image of the isolated fibril filament observed by negative-staining EM. Most filaments displayed the double-stranded state. (B) Averaged images from the selected 16,520 segmented images constructed using “2D classification” of RELION-3.0 (1). Images of the fibril filament were segmented at a pixel size of 160 × 160, with 90% overlap as a helical object. The 15 classes of the averaged image showed different interactions between two filaments. (C) Three-dimensional reconstruction of the double-stranded fibril filament using “*ab-initio* 3D” of cisTEM (2). I failed to converge the images to solid structures.

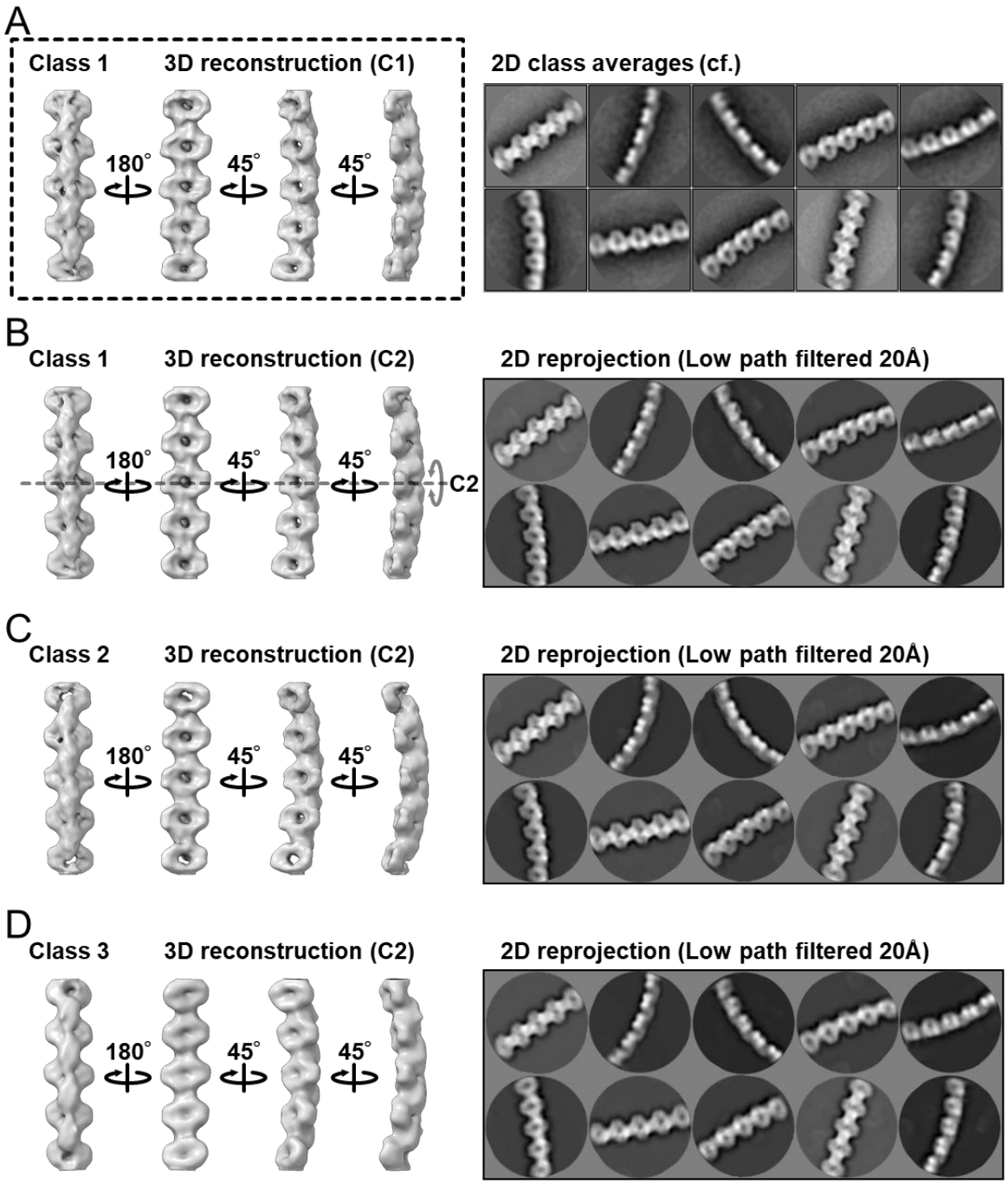

Supplementary Figure 3. Validation of the 3D structure of the fibril filament. (A) 3D structure reconstituted as C1 from 11,867 images obtained by negative-staining EM. Individual images represent the filament views from different angles. (B-D) Three classes of 3D structures reconstructed as C2. The density map (left in each panel) and its reprojection (right in each panel) are shown as viewed at different angles. As the C2 structure of class 1 aligned well with the C1 structure, I reconstituted the structures as C2. The reprojection was processed by a lowpass filter with a resolution of 20 Å. The reprojection images appeared similar to the averaged images classified into class 1, shown at the top right, suggesting that the density maps were successfully reconstituted.

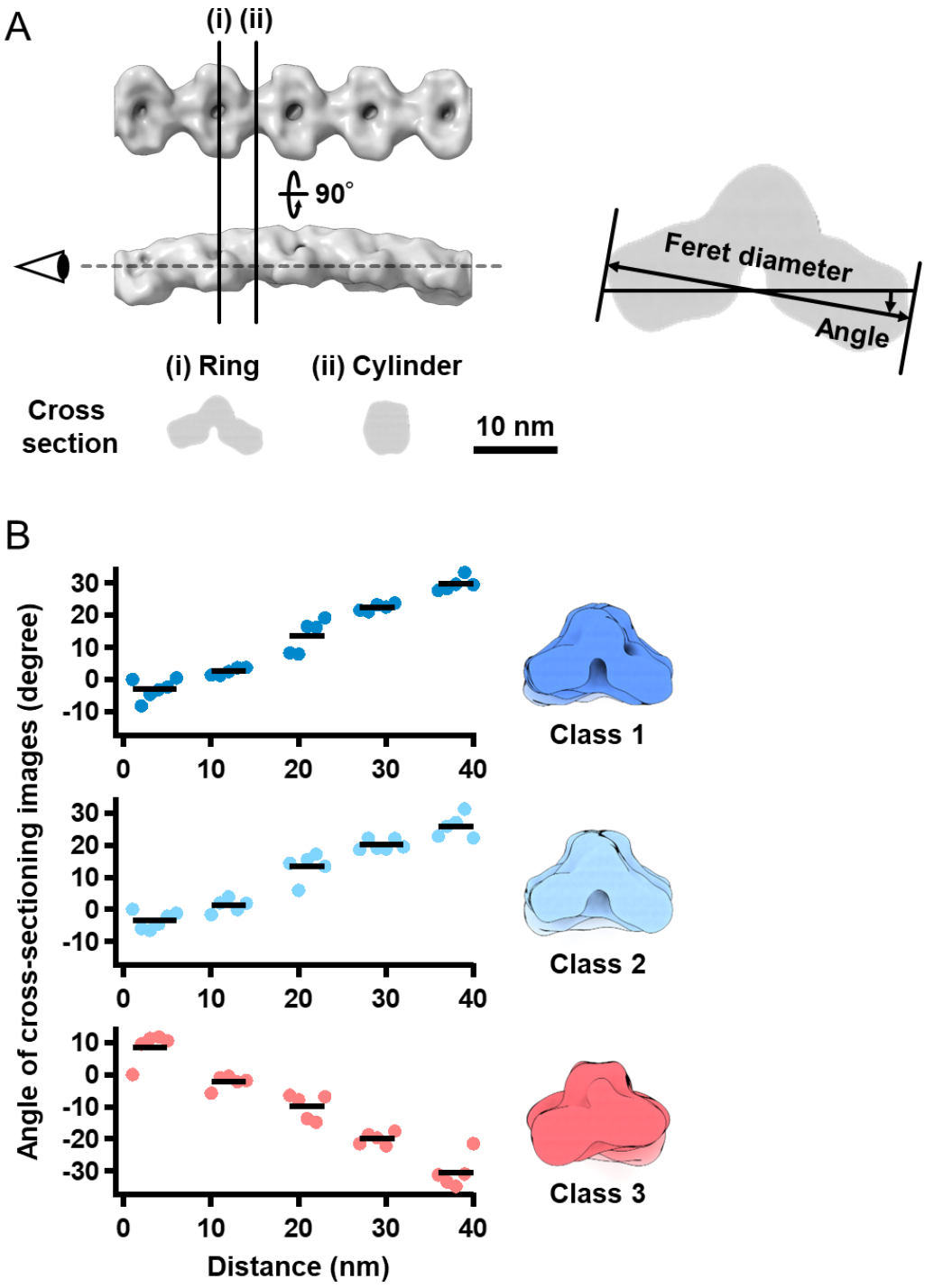

Supplementary Figure 4. Rotation of the repeated units along the filament axis in 3D structures reconstituted from negative-staining EM images. (A) Definition of the Feret angle. The cross-sections were reconstituted from the structures for ring (i) and cylinder (ii). The alignment of the longest axis was used as the Feret angle of ring. (B) Feret angles relative to the first angle plotted along the filament. The black bars indicate positions with a Feret diameter longer than 80% of the filament maximum.

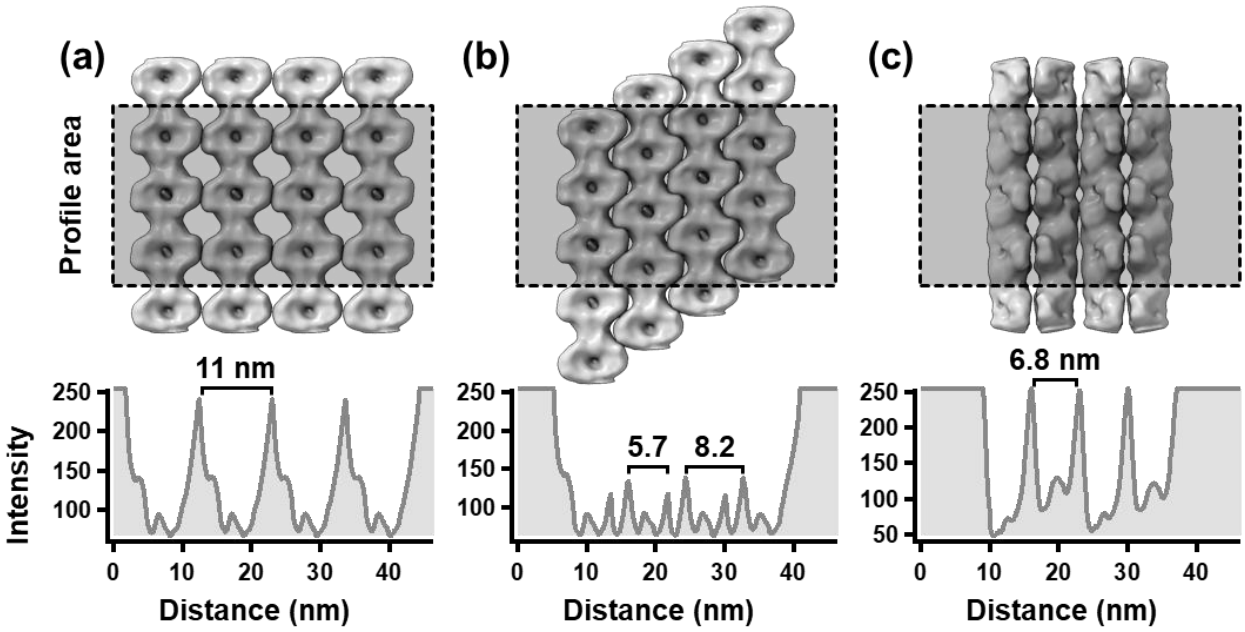

Supplementary Figure 5. Image profile of the ribbon predicted from 3D reconstructed models of the fibril filament. Upper panels show three types of interactions between fibril filaments. Lower panels show the image profiles of the gray boxed area in the upper panels. The peak intervals are 11.0, 5.7 and 8.2, and 6.8 nm for (a), (b), and (c), respectively. The experimental values were consistent with the values of 11.0 and 6.8 nm as shown in Fig. 2D (c).

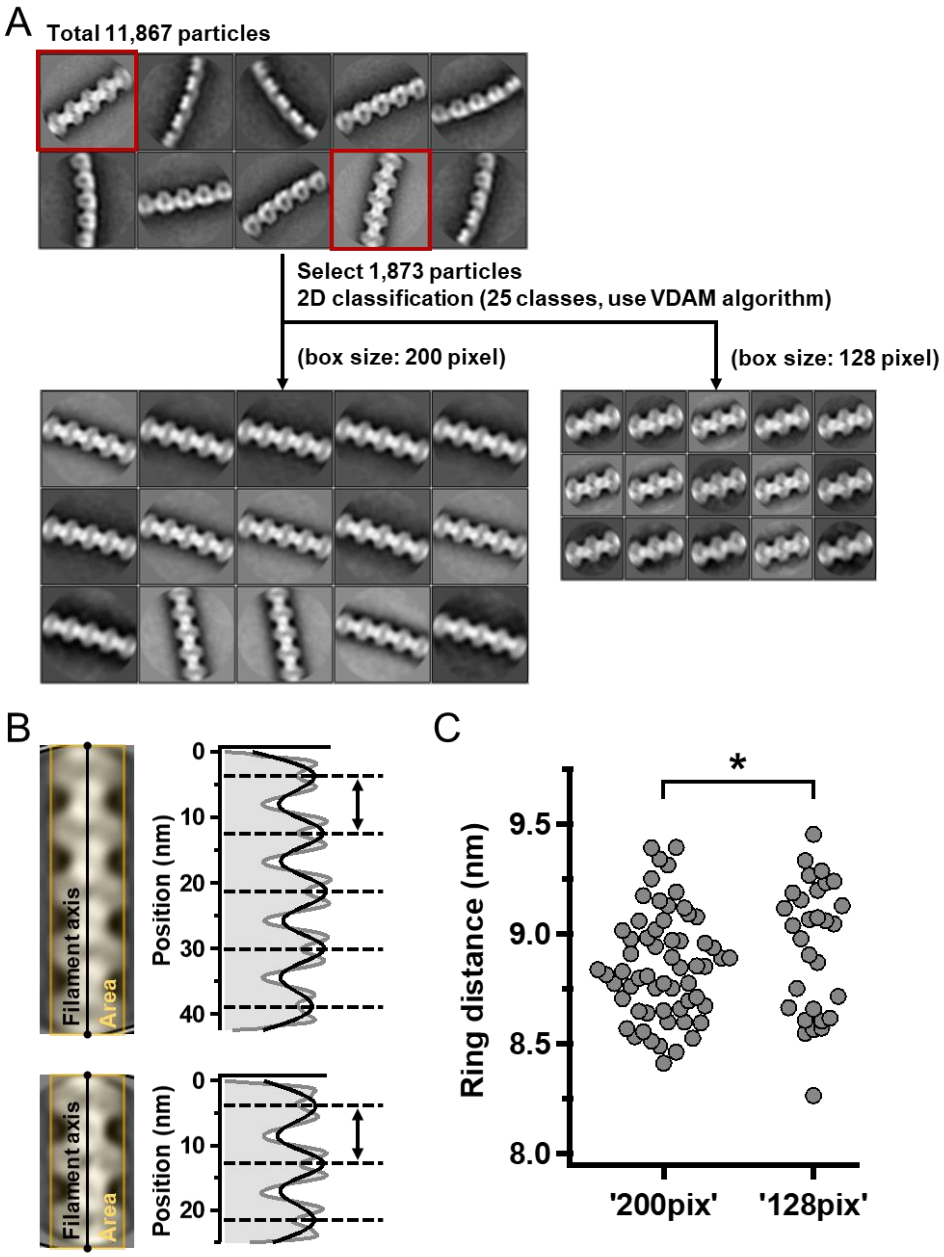

Supplementary Figure 6. Distribution of the ring intervals. (A) 2D classification of the fibril images with complete ring structures, as marked by red boxes in ten typical images (upper). Fifteen averaged images with complete ring were selected. The selected images were derived from 1,873 images, which were used for 3D reconstruction. Two box sizes, 200 and 128 pixels, were used to estimate the effect of box size on the calculation. (B) Measurement of the ring interval. Image profile was traced for the yellow boxed area 11 nm wide along the filament axis, as shown in the left images. The profile (gray line) and gaussian fitting (black line) are shown in the right graph. (C) Distribution of the ring intervals. The results did not differ between the 200 and 128 pixels box sizes. $^{*}p > 0.05$ (the agreements of the ring intervals between the box sizes were supported by Student's *t*-test). The results obtained from 200 pixels are summarized in Fig. 4C.

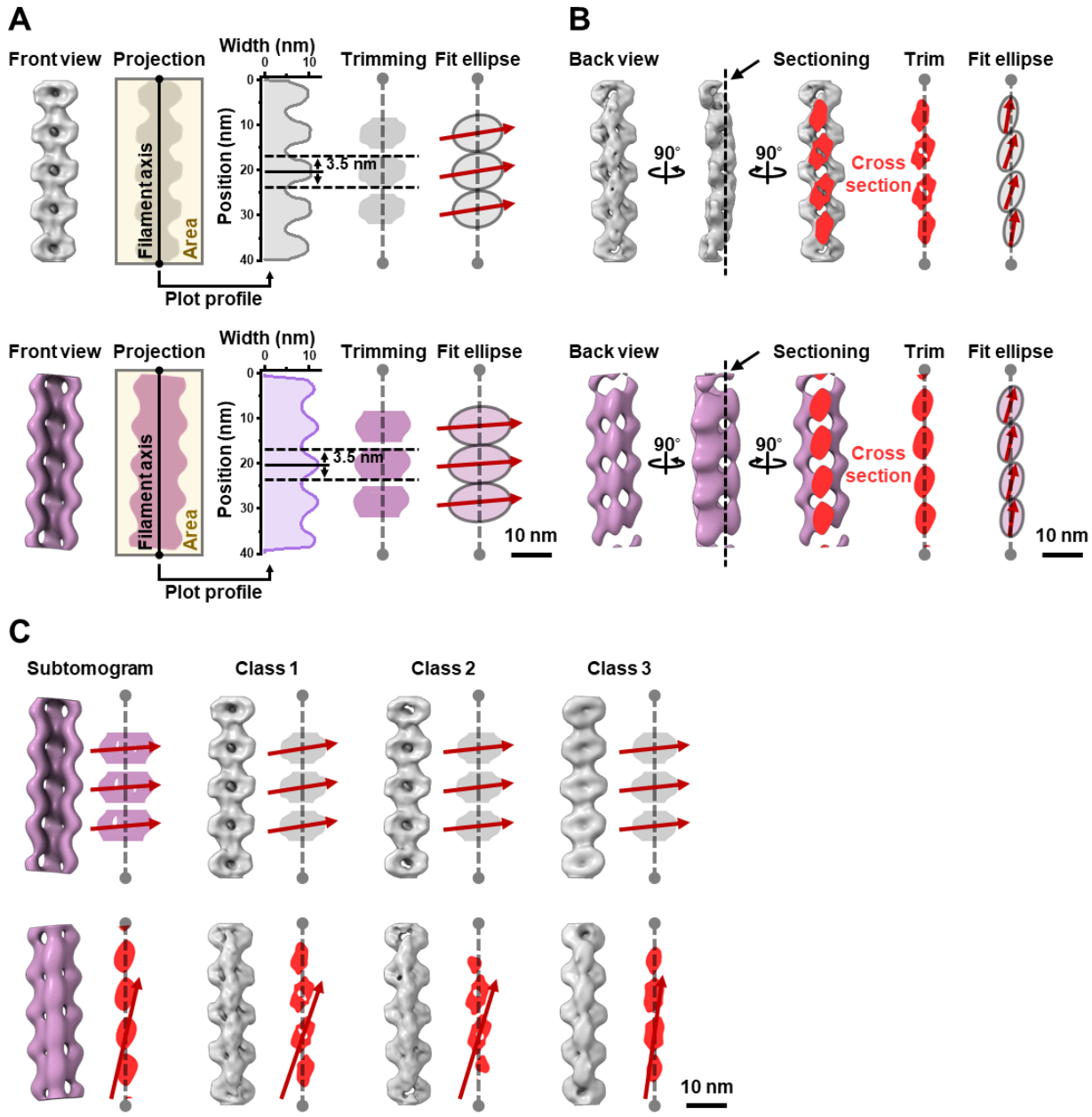

Supplementary Figure 7. Comparison of the handedness between images obtained from negative-staining and QFDE EM. (A) Alignments of ring parts relative to the filament axis. The 3D structures reconstituted from negative-staining (class1, grey) and QFDE (magenta) EM were projected, and the width was fitted by Gaussian function to detect the peak positions. The filament axis was determined using a function “relion_align_symmetry --sym d2” in RELION-3.0. The projection image was excised as images 3.5 nm high to both sides from the peaks, and fitted as ellipses. The long axes of ellipses are indicated by red arrows. (B) Alignments of the cylinder parts relative to the filament axis. The 3D structures reconstructed from negative-staining (grey, class 1) and QFDE EM (magenta) were sectioned at the plane shown by a broken line, and the sections were fitted as an ellipse. The long axes of ellipses are indicated by red arrows. (C) Summary of the ring and cylinder alignments in reconstructed filaments from negative-staining and QFDE EM methods.

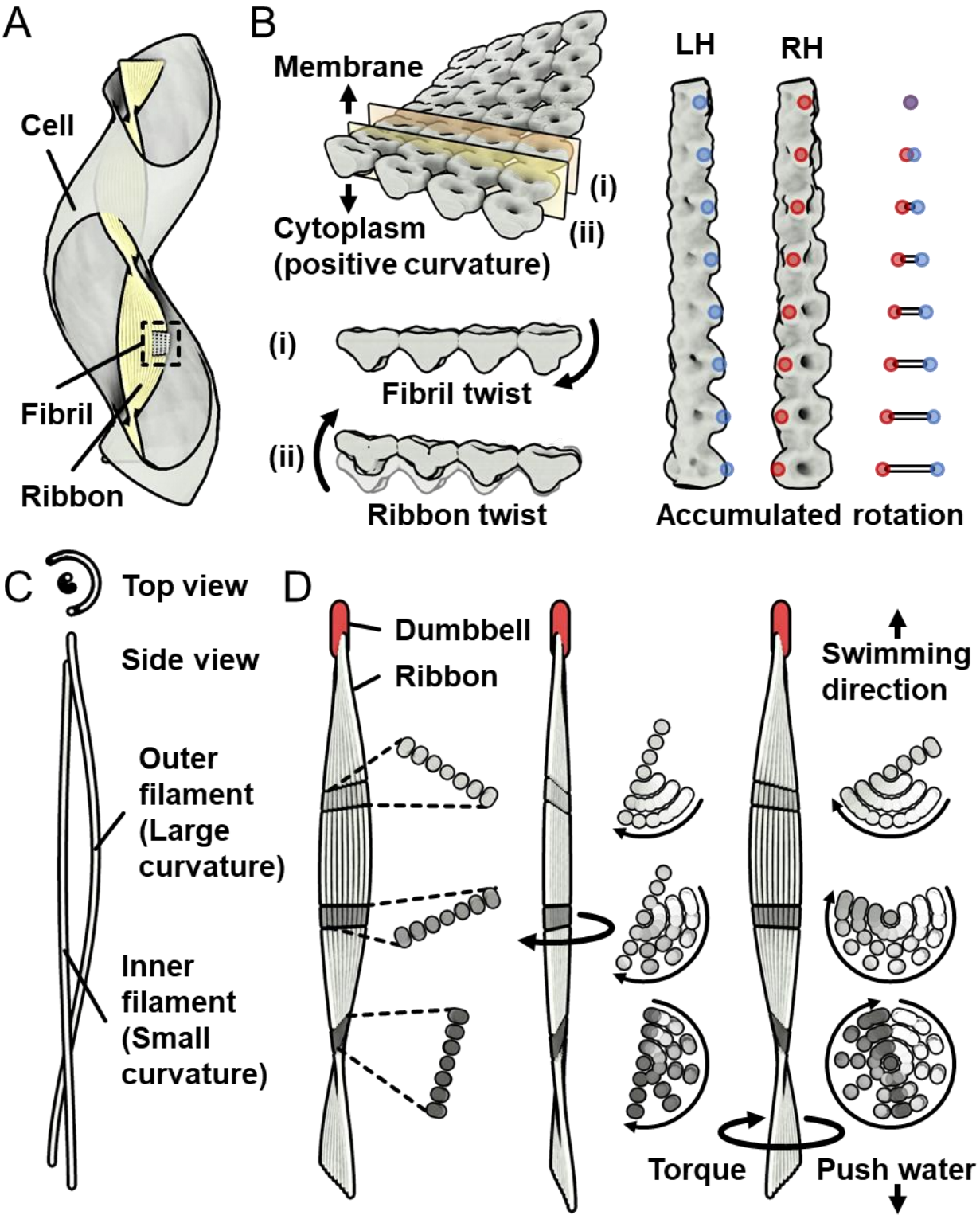

Supplementary Figure 8. Model schematic for swimming.

Supplementary Table 2. Peptide mass fingerprinting of band (v) in Fig. 2B.

SPE_1224 (MreB2)
Protein sequence coverage: 27%

matched peptides are shown in ***bold red***.

1 MANYKFGKEYSFLALDLGTANTVAYVAGQGIVYNEPSMMAYDTLSNSLVA
51 LGEEAYKMIGKTHDHIKMVTPLVDGVISDMDAAQDLLK**HIFGRLK**MTGIW
101 K**NSLVILACPSGVTELER**SALKAIAKDMGASYVLVEEEVKLAALGAGINI
151 GLAQGNLVIDIGGGTTDIAILSAGDIVKSKSVKVAGKHFDQEIQKYIR**AE**
201 **YNVLIGIR**TAEQIKKDIGALVKIVNEKPIRAFGR**DIITGLPR**EVMIKPEE
251 IK**NVLLAPFSRITDLLVEVLEETPPELAGDVIRNGITICGGGALIR**GIVK
301 **YFESIFQLK**VRAAQDPLMCVIDGAKTYEKNLGAVIERIELLEAKEYKI

Start	–	End	Mr(calc)	ppm	Peptide
89	–	95	869.5235	-18.6	K.HIFGRLK.M
102	–	118	1856.9666	-31.8	K.NSLVILACPSGVTELER.S
199	–	208	1146.6397	-29.3	R.AEYNVLIGIR.T
235	–	242	883.5127	-23.2	R.DIITGLPR.E
253	–	261	1015.5815	-37.3	K.NVLLAPFSR.I
262	–	283	2420.3050	-29.9	R.ITDLLVEVLEETPPELAGDVIR.N
284	–	296	1300.6922	-36.8	R.NGITICGGGALIR.G
301	–	309	1173.6070	-32.3	K.YFESIFQLK.V

SPE_1230 (MreB4)
Protein sequence coverage: 21%

matched peptides are shown in ***bold red***.

1 **MLDIVYVYTHWK**RKKGGIFTMAGFNSGKSKRPTFVSMDLGTANTLVYVSG
51 SGVVYNEPSIVAYRIKENR**IIAVGIEAYK**MIGKGNKSIR**IVRPMVDGVIT**
101 **DIR**ATEAQLRYIFGKLRISKQLKHSIMLLACPSVITELEKAALKKIAMNL
151 GATKVFVEEEVKMAALGGGVDIYKPTGNLVVDMGGGTTDIAVIASGDIVL
201 SKSVKVAGNYLNDEMQKFIRSQYGLEVGSKTAEQIKIEIGSLAKYPDERK
251 MKVYGR**DVVSGLPREIEVTPEEVR**EVLKVPVSRIIDLTVQVLEETPPELA
301 GDIFKNGITIYGGGALIKGIDRYFTDTLQLPSK**VGEQPLLAVINGTKKFE**
351 **SDIYDILR**QEQMHTKELDY

Start	–	End	Mr(calc)	ppm	Peptide
1	–	12	1582.7854	27.6	-.MLDIVYVYTHWK.R + Oxidation (M)
70	–	79	1075.6277	-34.4	R.IIAVGIEAYK.M
90	–	103	1598.8814	-33.6	R.IVRPMVDGVITDIR.A + Oxidation (M)
257	–	264	841.4658	9.77	R.DVVSGLPR.E
265	–	274	1199.6034	-33.1	R.EIEVTPEEVR.E
334	–	347	1437.8191	-48.0	K.VGEQPLLAVINGTK.K
348	–	358	1397.7191	-29.6	K.KFESDIYDILR.Q
349	–	358	1269.6241	-27.8	K.FESDIYDILR.Q

CHAPTER IiI

Cryo-EM structures of the cytoskeletal fibril in the swimming *Spiroplasma*

Keywords: Cryo-EM, Cryo-ET, Subtomogram averaging. Helical shape, Motility, Cytoskeleton, Filament, Single particle analysis.

Abstract:

Spiroplasma, belonging to the phylum Mollicutes, are parasitic or commensal bacteria that spread throughout the world. They can swim in a unique way in which the cells switch their helical cell body between left and right-handed pushing water backward. The helix is controlled by a ribbon structure composed of MreB, a member of the actin superfamily, and *Spiroplasma* specific fibril proteins in the cell. The fibril filament is composed of repeating rings connected by a cylinder, and the amino acid sequence of the N-terminal half of the fibril protein is approximately 20% similar to a bacterial SAH nucleosidase. In this study, single-particle cryo-EM of the isolated fibril filament revealed the structure at 3.6 A resolution, and the atomic structure of the fibril protein was constructed by modeling 512 amino acid residues. The N-terminal region with the sequence similarity to nucleosidase corresponded to a cylinder density and the other part corresponded to the ring, and the cylinder and ring each consisted of two subunits in two rotational symmetry. The corresponding parts of the nucleosidase shared the same overall shape and dimeric formation with the SAH nucleosidase. However, the structure of the active site was not conserved. The fibril filaments were rotationally symmetric and had a helical pitch of approximately 700 nm in their most extended state, similar to that of cells. The variation of the reconstructed filaments suggested that the fibril is flexible with the range of 300-680 nm in the helical pitch and 20-100 nm in the helical diameter. Cryo-ET of the *Spiroplasma* cells and syn3B, a minimal synthetic cell expressing MreB and fibril, revealed the localization of the each protofilament composing the ribbon in the cell. The fibril filaments were aligned so that the positively charged ring side was in contact with the inner side of the plasma membrane. The five MreB double-stranded filaments were aligned in the center of the ribbon with 2-3 fibril filaments on each side of the MreB sheet. These findings suggest that fibrils evolved from nucleosidase provide the ribbon with cooperatively, polarity, and robustness by mechanically supporting the structure and force generation of MreB.

One-Sentence Summary:

The fibril structures revealed by cryo-EM suggested the evolutionary origin of the fibril protein and functional roles in *Spiroplasma* swimming.

Introduction:

Spiroplasma sp., a member of the class Mollicutes characterized by small genome size, is *spread* throughout the world. They have a major impact on industry and other organisms, including plants such as corn and citrus fruits, as well as arthropods such as crabs and flies. One of the keys to the success of this bacterium may be its unique swimming mechanism, because the efficient migration directly leads to habitat expansion. This swimming is caused by switching the helical cell body between left- and right-handed. That is, the rotation of the cell helix behind the kink position caused by shifting the different helices pushes the water backward. The helix formation and helix switching in *Spiroplasma* is considered to be due to an internal structure called the ribbon. In addition, all Mollicutes bacteria lack PGs. The ribbon is composed of MreB, known as bacterial actin, and fibril, a protein specific to genus *Spiroplasma*. The recent study reported that expression of two types of *Sporoplasma* MreBs in the minimal synthetic bacterium syn3B, which is based on a Mollicutes bacterium, causes some cells to reconstruct a swimming behavior similar to that of *Spiroplasma*. This indicates that the conformational change of MreB is responsible for the force generation for the swimming. The fibril protein, another major component of the ribbon, is one of the most abundant proteins in *Spiroplasma* cell and is well conserved in the genus *Spiroplasma*, including amino acid sequence similarity of more than 90%. The helical pitch of the isolated fibril filaments was consistent with that of *Spiroplasma* cells. Interestingly, the N-terminal half of the fibril protein shares up to 20% similarity with SAH nucleosidase, which is essential for bacterial growth. These points raise questions about possible roles and evolutionary origins of the fibril protein in the *Spiroplasma* swimming and survival. To answer these questions, it is essential to understand the atomic structure of the fibril protein and their localization patterns in *Spiroplasma* cells. Previously, we succeeded in isolating fibril protein from *Spiroplasma* cells and revealed the low-resolution structure of the fibril filament. In this study, based on these experiences, we performed single-particle cryo-EM of the isolated fibril filament and cryo-ET of *Spiroplasma* cell and the minimal synthetic bacterium, syn3B, to solve the mystery of the fibril protein.

Result:

Single-particle cryo-EM of the fibril filament

We isolated fibril filaments from Spiroplasma cells using a previously established method and performed cryo-EM observation and single particle analysis. Since good images were obtained (Fig. 1a), segmented images of 300 nm length along the filaments were extracted with 90% overlap between consecutive segments, followed by 2D classification (Fig. 1b). The 3D image was then reconstructed from 147,040 such segmented images. The resulting structure had a resolution of 3.6 A with a Fourier shell correlation of 0.143 (Supplementary Fig. 1 and 2). Based on the cryo-EM map, an atomic model of the six subunits of the fibril protein was constructed (Fig. 1c-d). To estimate the helical pitch and handedness of the fibril filament, we constructed a long 3D density map of the fibril filaments

by extending the short segment map to a length of 1/2 helical pitch (Fig. 1e). The reconstructed fibril filament was left-handed, and the 1/2 helical pitch was approximately 350 nm. The shape of the fibril filament was characterized by the rings with a 105 A long axis, connected by the cylinders with 89 A spacing (Fig. 1c). These characteristics of the fibril filament were consistent with the structure previously revealed by our negative staining electron microscopy.

Atomic structure of the fibril filament

Atomic modeling was performed with the EM map at 3.6A resolution, and 512 residues of amino acids were correctly assigned (Fig. 1d, Supplementary Fig. 2). The amino acid sequence of the fibril protein can be divided into the N-terminal 228-residue sequence with approximately 20% similarity to SAH nucleosidase and the C-terminal sequence. The atomic model of the fibril filaments showed that the 228 residues on the N-terminal side mainly corresponded to the cylinder, while the rest of the C-terminal region mainly corresponded to the ring (Fig. 1d). There were three major interaction surfaces (i)-(iii) between each subunit in the fibril filament, and each interface oriented many non-polar side chains (Fig. 2a). The interface (i) consists of three α-helices, including four non-polar side chains and three polar side chains (Fig. 2a). The interface (ii) consists of four loops, including eight non-polar side chains and two polar side chains (Fig. 2a). The interface (iii) consists of four β-sheets and one loop, including 13 non-polar side chains (Fig. 2a). These interactions suggest that the fibril filament is a more elastic and robust filament than exhibits polymerization-depolymerization dynamics.

The structure of the fibril protein was compared to the SAH nucleosidase structure from Bacillus subtilis (Fig. 2b, Supplementary Fig. 3). The adenine-binding site of the nucleosidase contains two β-strands, an α-helix, and a loop. This site consists of the residues Glu175, Arg194, Ser197, and Asp198. In contrast, in the fibril protein, the residues corresponding to the adenine binding site of the nucleosidase were mutated to Glu171, Lys190, Tyr193, and Asn197, respectively (Supplementary Fig. 3). In addition, the VAL335-LYS347 chain, a part of the C-terminal domain within the same subunit, were bound to the pocket of the adenine-binding site (Fig. 2b, Supplementary Fig. 3). The α-helix corresponding to Met10- Gly22 in SAH nucleosidase formed a β-strand with VAL333-ASN336 in the fibril protein (Supplementary Fig. 3). We concluded that the fibril protein lost the nucleosidase activity.

Structural flexibility of the fibril filament

To investigate structural changes in the fibril filament, we tested whether structural variations could be obtained by further single particle analysis. Therefore, the 147,040 particles from the high-resolution EM map used for atomic modeling were re-extracted with a box size of 450 nm containing 10 fibril subunits. From these particles, a 2D classification was performed to sort out the

fibril filaments that were possible single-stranded fibrils. The resulting 81,139 particles were subjected to 3D variability analysis in the cryoSPARC software. The structural changes of the fibril filaments were specified by continuous movements in three directions, and two of them showed distinct movements. One was characterized as a forward bending toward the ring, and the other was characterized as a left and right bend with the ring in front (Fig. 3a-b). These flexibilities allow fibril filaments to have helical pitches and diameters in the range of 300-680 nm and 20-100 nm, respectively (Fig. 3c).

Cryo-ET of the internal ribbon

We attempted to analyze the internal ribbon structure composed of MreB and Fibril by cryo-ET of *Spiroplasma* cells. *Spiroplasma* cells suspended in PBS were applied to EM grids, blotted from one side of the grid, and rapidly vitrified in liquid ethane. The prepared grids were imaged by cryo-EM in continuous tilt. The motion-corrected tilt series were aligned, and the three-dimensional tomograms were reconstructed. The reconstructed tomograms of the *Spiroplasma* cells visualized the internal ribbon structure running the entire length of the helical cell body (Fig. 4a). The ribbon was characterized as a sheet structure consisting of several protofilaments in top view, and inside view, the ribbon was bound to the cell membrane sensing positive curvature, suggesting that the ribbon is localized in the innermost line of the helical cell body (Fig. 4a).

To understand how protofilaments are organized in the native ribbon of *Spiroplasma*, cryo-ET of syn3B cells expressing MreB4-5 or the fibril protein was also performed in the same way. The sheet-like ribbon structures binding to the plasma membrane were also observed in syn3B cells expressing either MreB4-5 or fibril (Fig. 4c). The ribbons covering the cell length were obtained, although not as long as those of *Spiroplasma*, and their helical pitches and handedness were measured. All of the ribbons observed in *Spiroplasma*, syn3B MreB4-5 strain, and syn3B fibril strain had 1/2 helical pitches of about 300 nm (Fig. 4b). However, both left- and right-handedness were observed in *Spiroplasma* and syn3B Mreb4-5 strain, whereas only left-handedness was observed in syn3B fibril strain (Fig. 4b). The distance between the protofilaments forming the MreB sheet structure was 5 nm, while the distance in the fibril sheet structure was 10 nm (Fig. 4c). Based on these results, we re-analyzed the native ribbon of *Spiroplasma* and found that 2-3 fibril filaments with 10 nm spacing line both sides of the 5 nm spaced MreB sheets (Fig. 4c).

Subtomogram averaging of the *in situ* fibril filament

To clarify the intracellular structure of the fibril filament, we performed a subtomogram averaging following cryo-ET of syn3B expressing the fibril protein (Supplementary Fig. 4 and 5). The fibril filaments in syn3B cells formed sheet-like structures with adjacent fibers in contact with the plasma membrane (Fig. 5a). From the tomograms obtained, the coordinates of the subtomograms

corresponding to the ring spacing along the fibril filaments were manually obtained. The extracted particles were sorted by 2D and 3D classification, and finally a EM map with a resolution of 16 A was obtained from 5182 particles. The resulting structure had each ring facing the plasma membrane and the cylinders facing the cytoplasm, forming a sheet structure with the adjacent fibril filaments (Fig. 5b-c). The atomic structure fitting revealed that the side chains between adjacent fibril filaments were oriented to cancel the electric charges each other at the closest C-terminal domains (Fig. 5c). The interface between the fibril filament and the plasma membrane through the ring portion was characterized by the orientation of 14 positively charged residues of the fibril protein that interacted electrostatically with the phosphate groups of the lipid (Fig. 5c).

Discussion:

Since no structure similar to the C-terminal region of the fibril protein was found based on amino acid sequence or 3D structure (Fig. 1d), no evolutionary origin was suggested by this study. On the other hand, the N-terminal domain of the fibril protein obtained in this study supports the idea that the structure originated from a nucleosidase and became the fibril with a completely different function (Fig. 2b). The phylogenetic tree showing the evolution from nucleosidase to fibril (Supplementary Fig. 3a), based on their amino acid sequences, unexpectedly suggested that the fibril protein is more closely related to other Mollicutes nucleosidases than to *Spiroplasma* nucleosidases. This may mean that the fibril was acquired and spread by horizontal gene transfer from a Mollicutes bacterium other than *Spiroplasma* sp.

The structural flexibility of the fibril filament, suggested by the variation in the reconstructed images, was observed in two directions (Fig. 3a-b). However, this is because the structural variations were examined in only two directions, and fibril fibers are actually expected to be flexible in a combination of these directions (Fig. 3a-b). Given that the fibril filament is not easily depolymerized and that sonication causes only partial cleavage, the fibril filaments are thought to have a flexible, spring-like property that supports the helical shape of the cells and the helical conformations. The proposed structural changes of the fibril filaments are continuous and do not involve periodic helicity switching (Fig. 3b). The fact that the fibril filament extends the entire length of the cell and that the helical shift propagates along the entire length during *Spiroplasma* swimming would expect a reversal of handedness in the fibril filaments, but the experimental results are not consistent with this. Perhaps the helical switching of the fibril filaments only occurs when a force is applied in a specific direction, either directly by the MreB proteins or through a structure such as a membrane.

When syn3B expresses MreB4 and MreB5, it forms a helical cell shape similar to *Spiroplasma* cells, swimming by switching the helix between the different handedness, although at a lower ratio. The expression of the fibril protein in the synthetic bacterium also forms a helical cell shape similar to *Spiroplasma* cells (Fig. 4b). Considering these facts and the results of the present study, it is

possible that the fibril filament may contribute to the primitive movement of MreBs by providing processivity, robustness, and efficiency. *Spiroplasmas* have no PG and their physical strength is weaker than Spirochetes. Fibrils may be present in fragile cells to resist the high mechanical stress caused by the helical shift. Indeed, many cells in synthetic bacteria expressing MreB4 and MreB5 showed irregular shapes. In this study, we observed three proteins, MreB4, MreB5, and fibril, expressed in syn3B, and were able to characterize the structure of each protein in the cell (Fig. 4b). The synthetic bacterium syn3B, as a minimal cell, is mainly used to study the integration of living systems. However, the small size of syn3B cells makes them suitable for tomography, and all the candidate structures inside are known (Fig. 4b). Therefore, when other biomolecules are expressed in syn3B, it may be possible to observe the intracellular structures formed by these molecules using cryo-ET.

Materials and Methods

Bacterial strains and culture conditions. JCVI-syn3B (GenBank: CP069345.1) and *Spiroplasma eriocheiris* (TDA-040725-5T) were cultured in SP4, SP4 media at 37 °C, 30 °C, respectively.

Cryo-EM and image processing. A 1.4 μl sample solution was applied onto a glow discharged holey carbon grid (Quantifoil R1.2/1.3 Mo grid, Quantifoil Micro Tools, Germany), and the grid was plunge-frozen into liquid ethane by Vitrobot mark IV (Thermo Fisher Science, USA) with a blotting time of 3 s at 18 °C and 90% humidity. All the data collection was performed on a prototype of CRYO ARM 200 (JEOL, Japan) equipped with a thermal field-emission electron gun operated at 200 kV, an Ω-type energy filter with a 20 eV slit width and a K2 Summit direct electron detector camera (Gatan, USA). An automated data acquisition program, JADAS (JEOL, Japan), was used to collect cryo-EM image data, and pre-processing, motion correction, and CTF estimation were carried out in real-time by the Gwatch image processing pipeline software we developed. Movie frames were recorded using the K2 Summit camera at a calibrated magnification of ×4,000 corresponding to a pixel size of 1.5 Å with a defocus range from −0.6 to −1.8 μm. The data were collected with a total exposure of 10 s fractionated into 60 frames, with a total dose of ~50 electrons Å−2 in counting mode. A total of 720 movies were collected.

Motion correction was performed by MotionCor2 and CTF parameters were estimated by Gctf. Fibril filament images were automatically selected by RELION 3.0 as helical objects and segmented into 200 x 200 pixel boxes with 90% overlap. After 2D classification of these segmented images by RELION 3.0, the best particles were selected from the results. 237,690 segmented images were 3D classified into four classes, and 147,040 segmented images from the best two classes were merged and 3D auto-refine was performed. Atomic model construction was performed in COOT28 followed by real-space refinement using

PHENIX29 . All 3D maps and model images used in this paper were created with UCSF ChimeraX.

Cryo-ET and image processing. A 3.0 µl sample solution containing 10 nm colloidal gold was applied onto a glow discharged holey carbon grid (Quantifoil R1.2/1.3 Cu grid, Quantifoil Micro Tools, Germany), and the grid was plunge-frozen into liquid ethane by Vitrobot mark IV (Thermo Fisher Science, USA) with a blotting time of 3 s at 4 °C and 90% humidity. All the data collection was performed on a CRYO ARM 300 II (JEOL, Japan) equipped with a cold field-emission electron gun operated at 300 kV, an Ω-type energy filter with a 20 eV slit width and a K3 Summit direct electron detector camera (Gatan, USA). Movie frames were recorded using the K3 Summit camera at a calibrated magnification of ×55,000 corresponding to a pixel size of 2.343 Å with a defocus range from −0.6 to −1.8 µm. The data was acquired at a tilt range from −60 to 60 degrees using a dose-symmetric tilt scheme at 3° increment.

Motion correction was performed by RELION's own implement and CTF parameters were estimated by ctffind4. Tilt series alignment and tomogram generation were performed in IMOD. Subtomogram coordinates were manually selected by 3dmod tool in IMOD. After 2D classification of these segmented subtomogram by RELION 4.0, the best particles were selected from the results. 21,973 segmented subtomograms were 3D classified into three classes, and 5,182 segmented subtomograms from the best one classe were selected and 3D auto-refine was performed. All 3D maps and model images used in this paper were created with UCSF ChimeraX.

Figure and legends

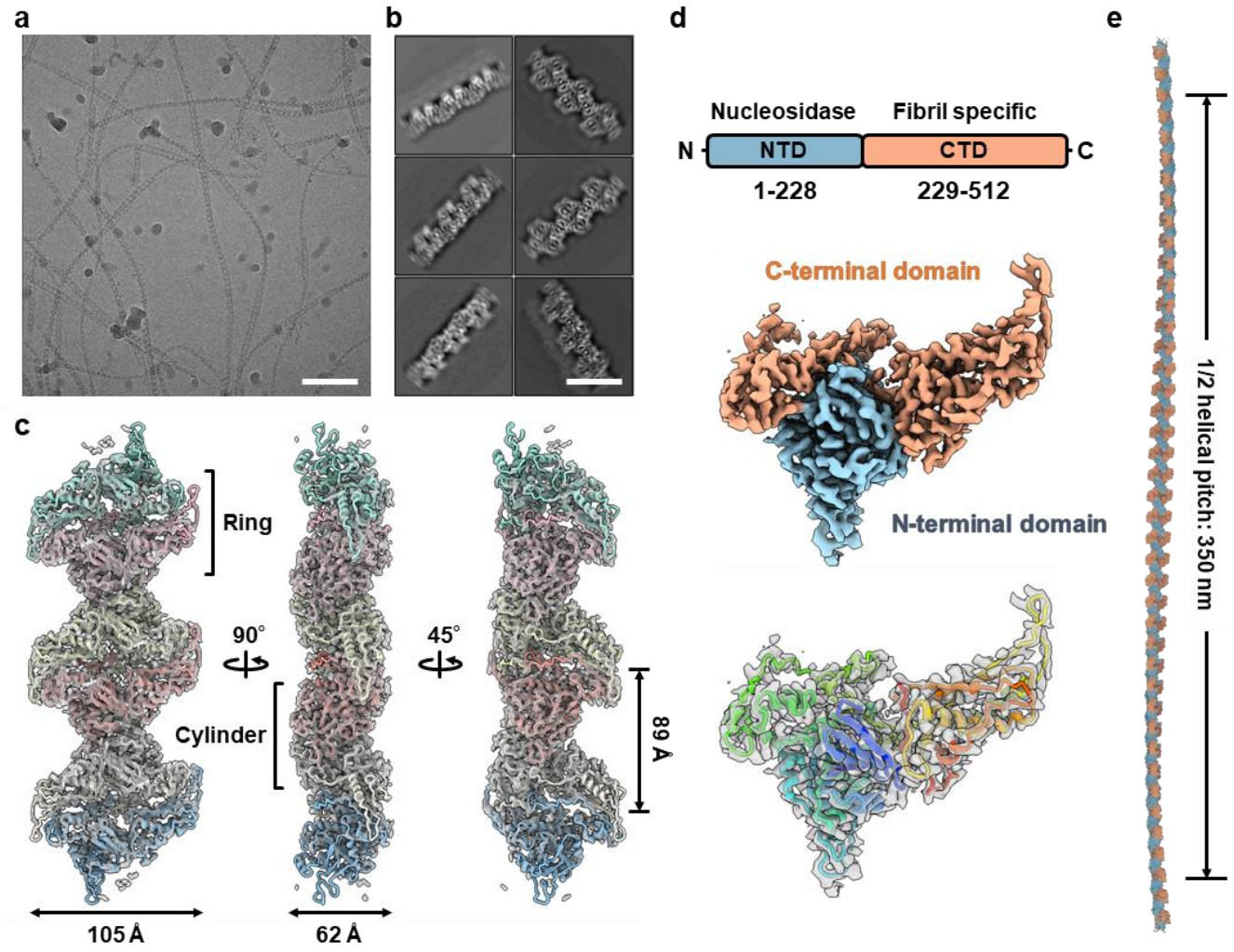

Fig. 1: Single-particle cryo-EM of the fibril filament.

a A cryo-EM image of ice-embedded fibril filaments. Scale bar, 100 nm. **b** Class averages by 2D classification. Scale bar, 15 nm. **c** Reconstructed density map and atomic models of the fibril filament. Each fibril subunit is colored differently. **d** domain structure of the fibril protein (upper). EM density map of a fibril subunit (middle). N-terminal domain (NTD) and C-terminal domain (CTD) are colored by blue, orange, respectively. EM density map and an atomic model of the fibril protein in ribbon representation colored in rainbow from the N- to C-terminus (lower). **e** a density map of the fibril filament extended to the length of 1/2 helical pitch.

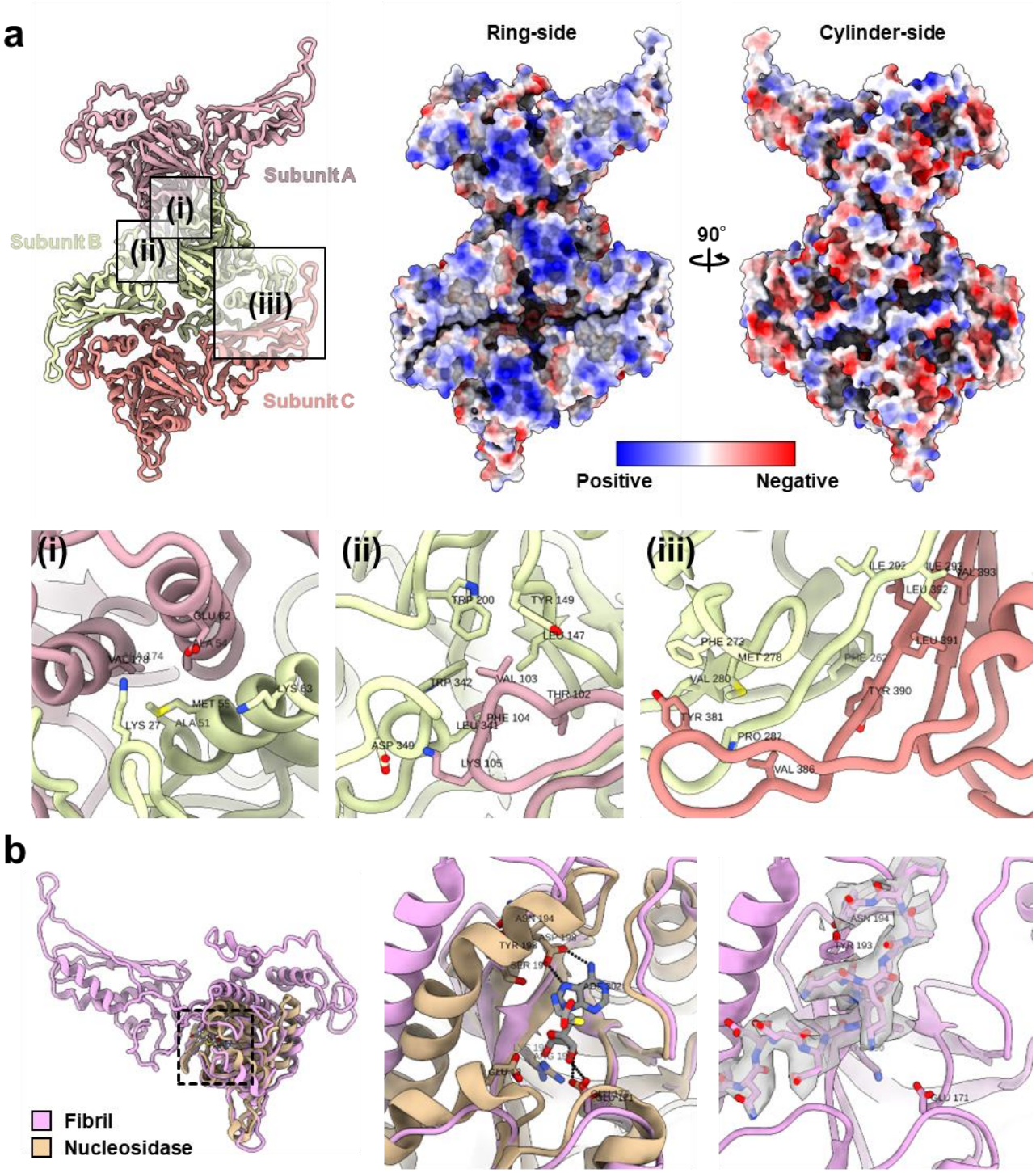

Fig. 2: Atomic structure of the fibril filament.

a Atomic structures of the fibril filament composed of three subunits (left-upper). The areas enclosed by squares are enlarged below. Surface model colored by the electrostatic potential at pH 7.0 (middle-, right-upper). **b** Superposing of the fibril protein (pink) and the nucleosidase (beige). The area enclosed by dashed squares is enlarged right. A part of the EM density map is shown as gray and translucent.

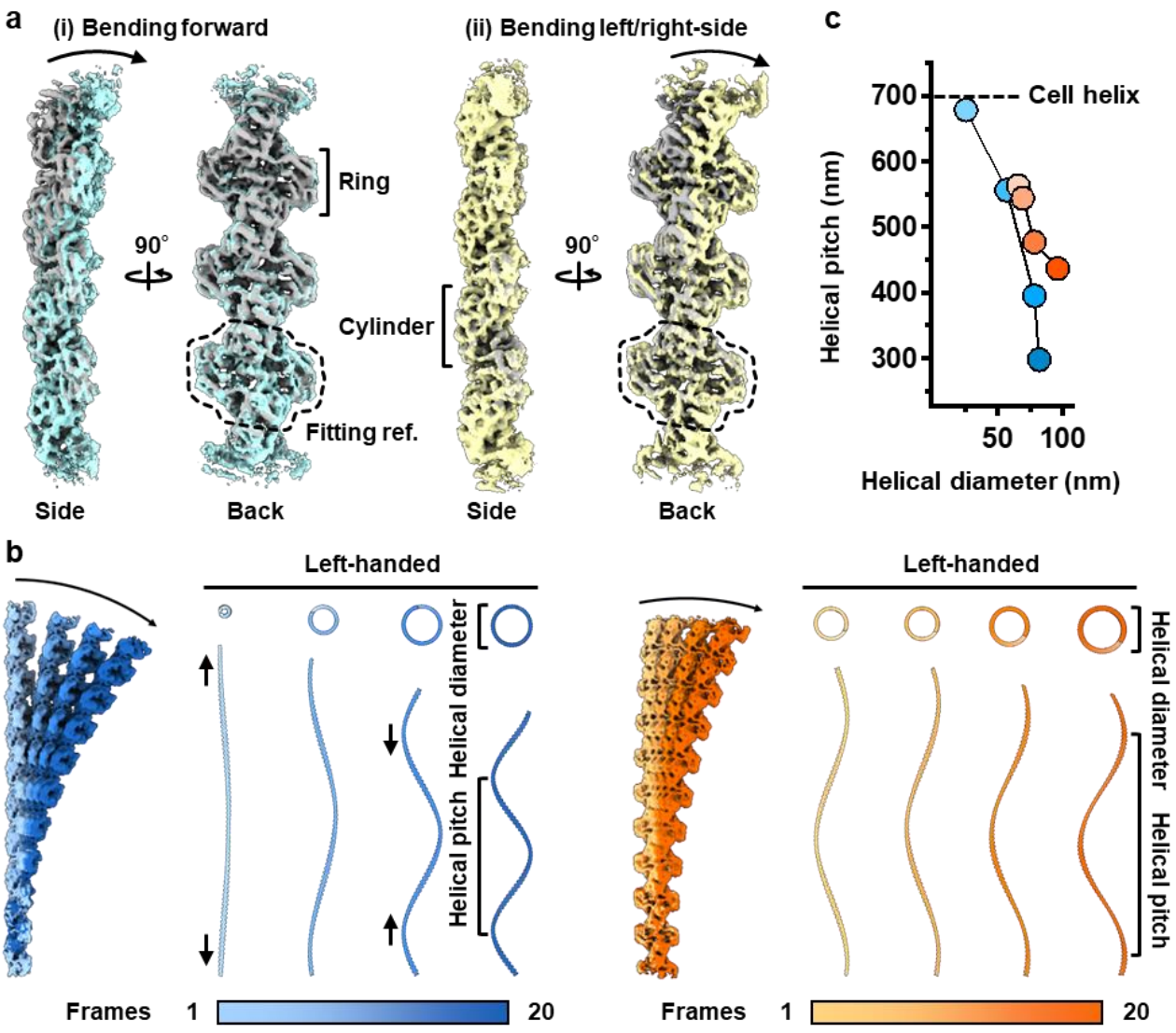

Fig. 3: Structural flexibility of the fibril filament.
a EM density maps reconstructed by cryoSPARC 3d variability alanysis. A default fibril filament (gray), the bending forward filament (blue), bending left-/right-side filament (orange) are shown**.** Dashed line indicates a fitting reference position for each density map. **b** Stitched volumes of straight and bend maps from a. Arrows indicate a spring like extension and contraction of the fibril filament. Helical pitches and diameters corresponding to each frame are listed. **c** relation between the helical pitches and diameters.

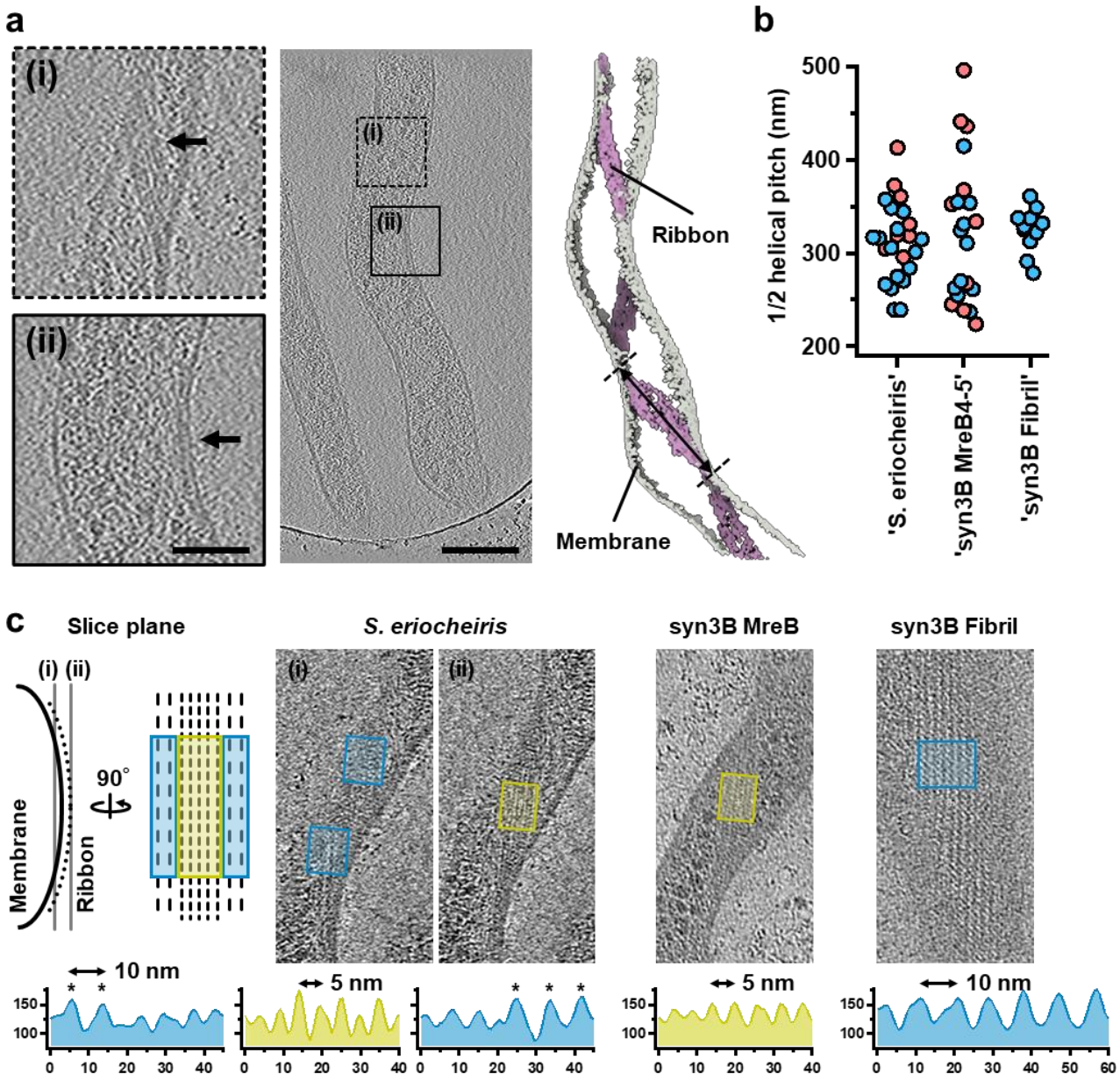

Fig. 4: Cryo-ET of the internal ribbon structure.
a Slice image from cryo-ET of *Spiroplasma* cell (middle). The areas enclosed by the squares are enlarged to the left. Solid and dotted squares are slices at different heights. Arrows indicate the typical ribbon appearance. Tomogram rendering is shown in the right. Bidirectional arrow indicates the 1/2 helical pitch of the ribbon. **b** 1/2 helical pitches of the ribbon in *Spiroplasma*, syn3B expressing MreB4-5 or fibril protein. Red and blue plots indicate right- and left-handedness, respectively. **c** Structural comparison of the ribbon in *Spiroplasma* cells and syn3B expressing mreB4-5 or Fibril strains. Each profiles for protofilaments is measured at box areas on tomogram slice images.

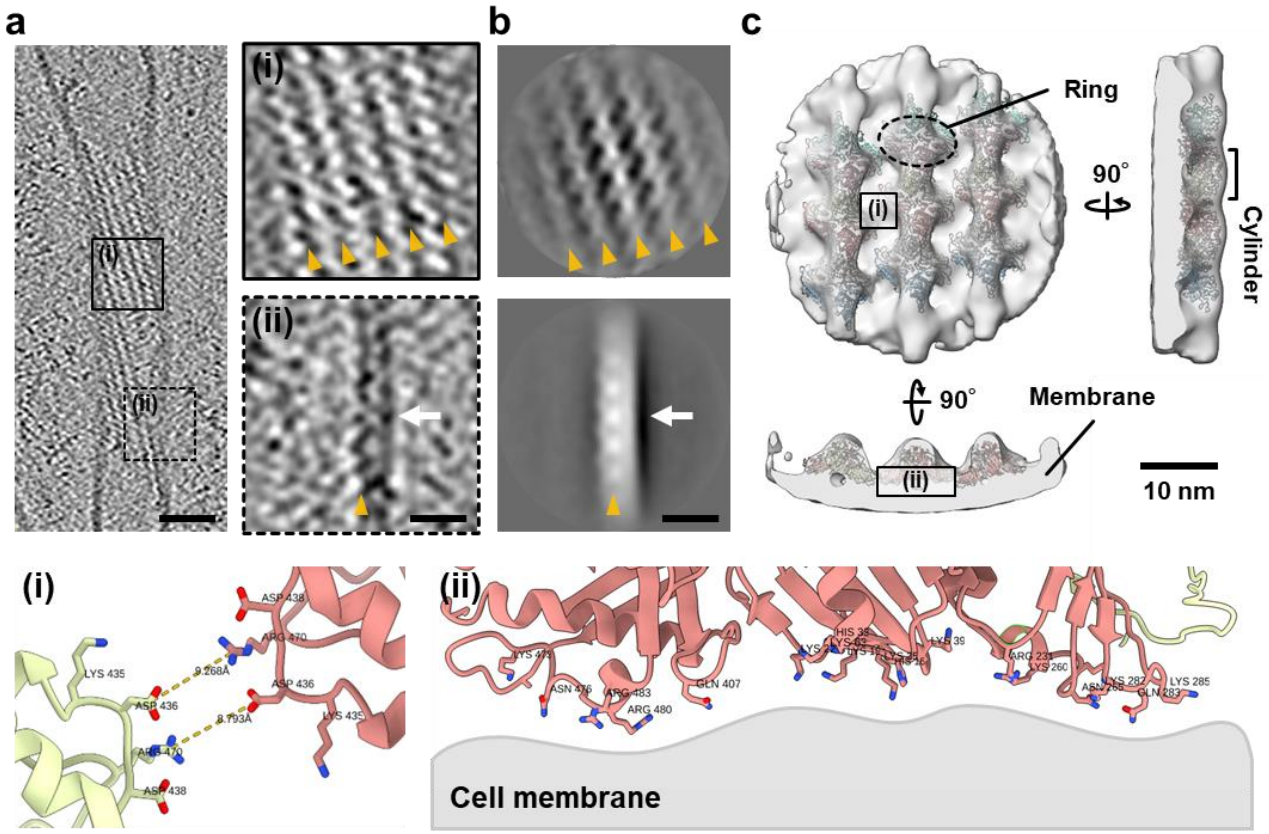

Fig. 5: Subtomogram averaging of the *in situ* fibril filament.
a Tomogram slice of syn3B cell expressing the fibril protein. The areas enclosed by the squares are enlarged to the right. Solid and dotted squares are slices at different heights. Yellow arrow heads indicate each fibril filament. White arrow indicates the plasma membrane. **b** Projection images of subtomogram averages. Yellow arrow heads indicate each fibril filament. White arrow indicates the plasma membrane. **c** Subtomogram average of the *in-situ* fibril filament at 16 Å resolution. The atomic structures of the fibril filament are fit in the EM map. Each fiber subunit is colored differently. The areas enclosed by squares are enlarged below.

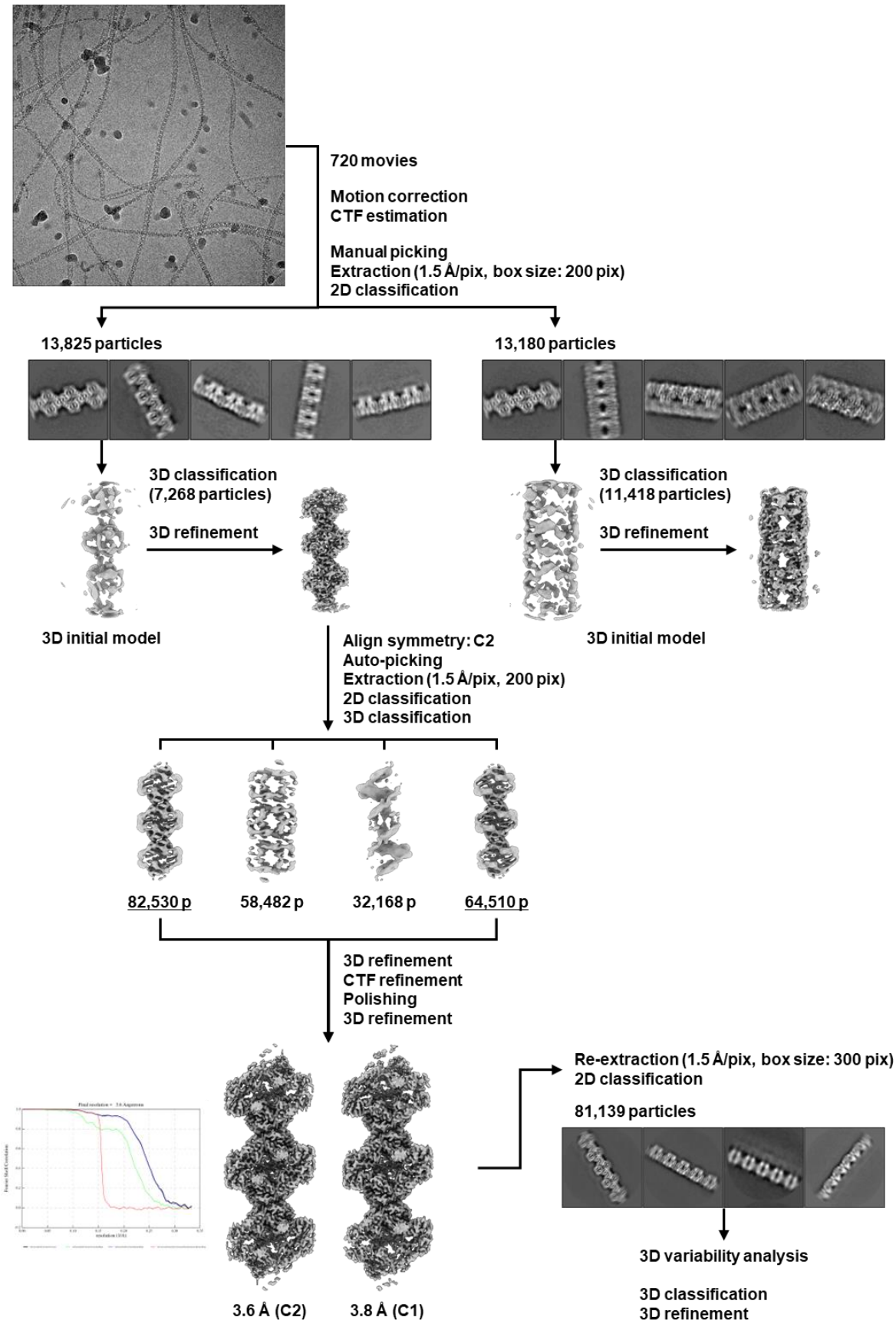

Supplementary Fig. 1: Single-particle analysis of the fibril filament.

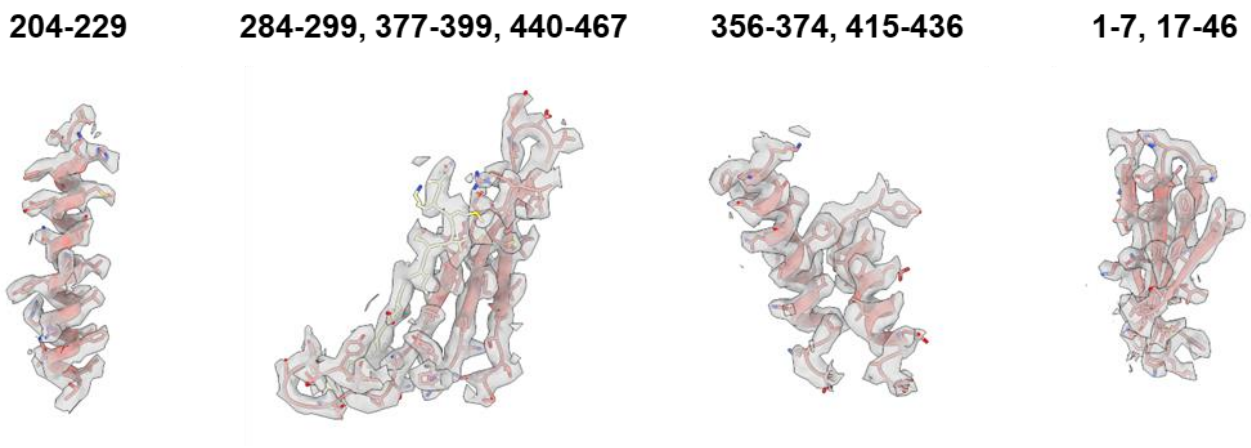

Supplementary Fig. 2: Cryo-EM maps and models of the fibril protein.
Atomic model with representative maps at 3.6 Å resolution. The numbers indicate the amino acids residues.

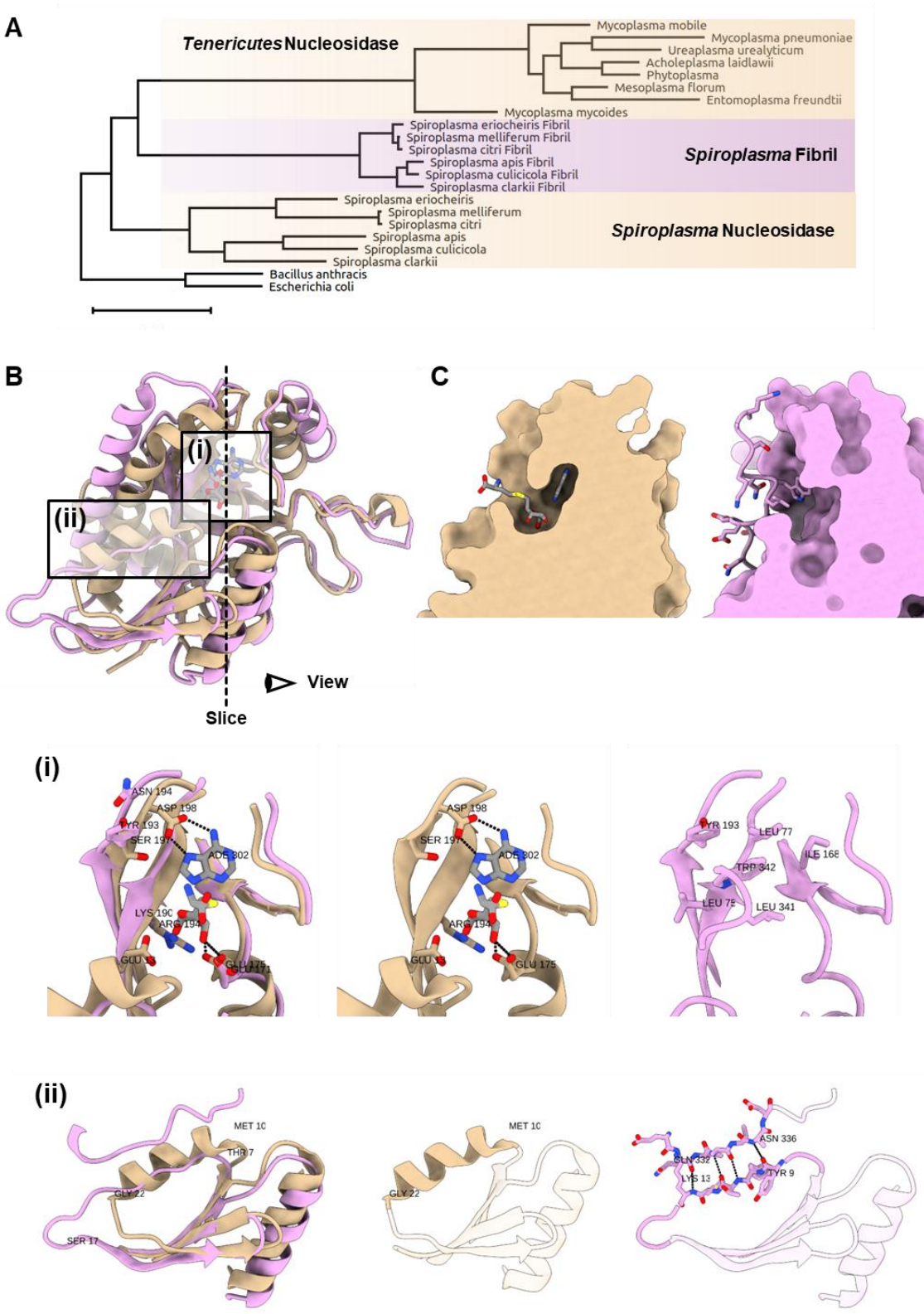

Supplementary Fig. 3: Structural comparison between the fibril protein and bacterial SAH nucleosidase. A a phylogenetic tree of the evolution from the nucleosidase to the fibril protein. **B** Superposing of the fibril protein (pink) and the nucleosidase (beige). The areas enclosed by squares are enlarged below. **C** Structural comparison of the enzymatic activity pockets by surface models.

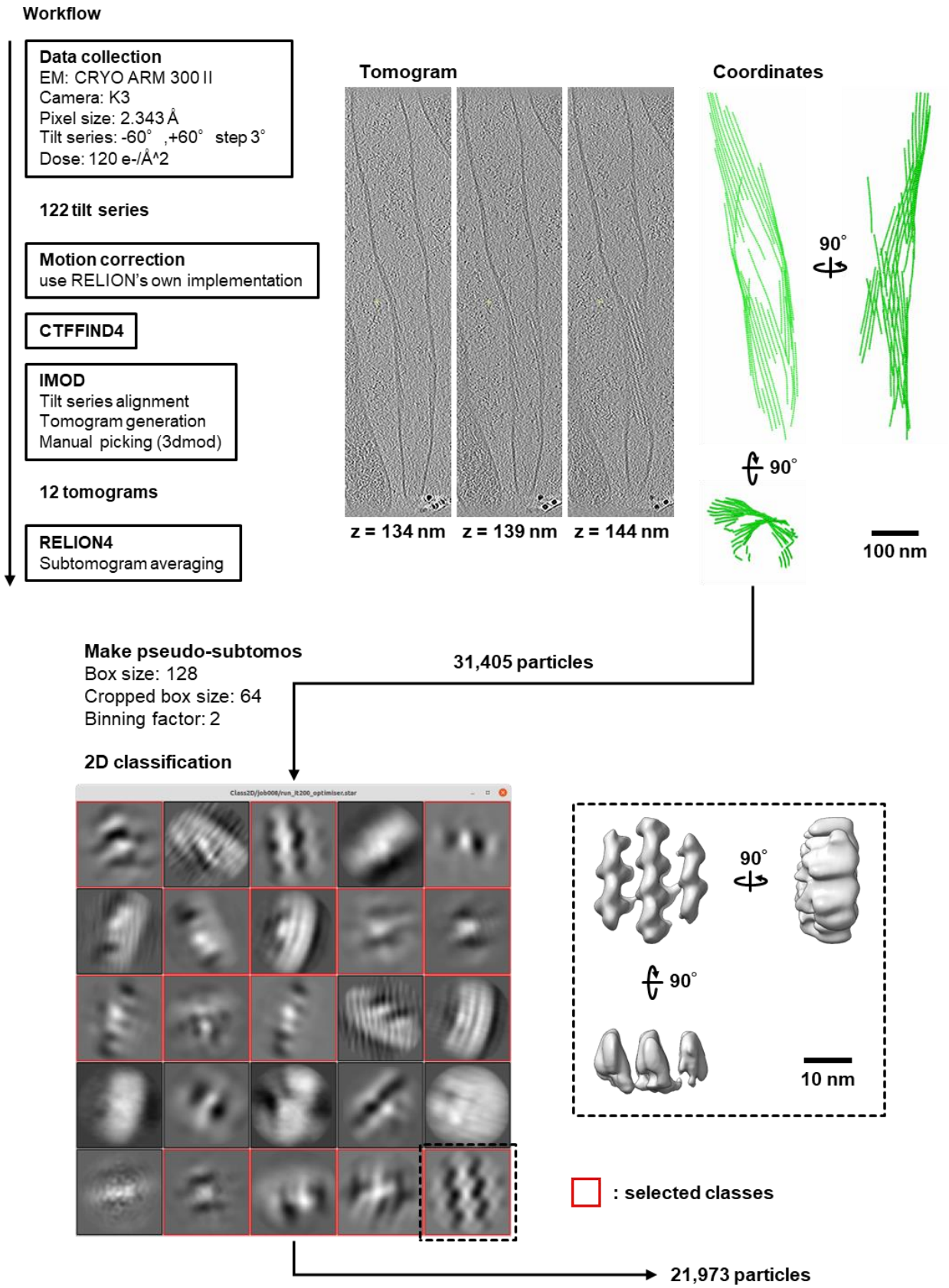

Supplementary Fig. 4-1: Workflow of cryo-ET and subtomogram averaging of the *in situ* fibril filament.

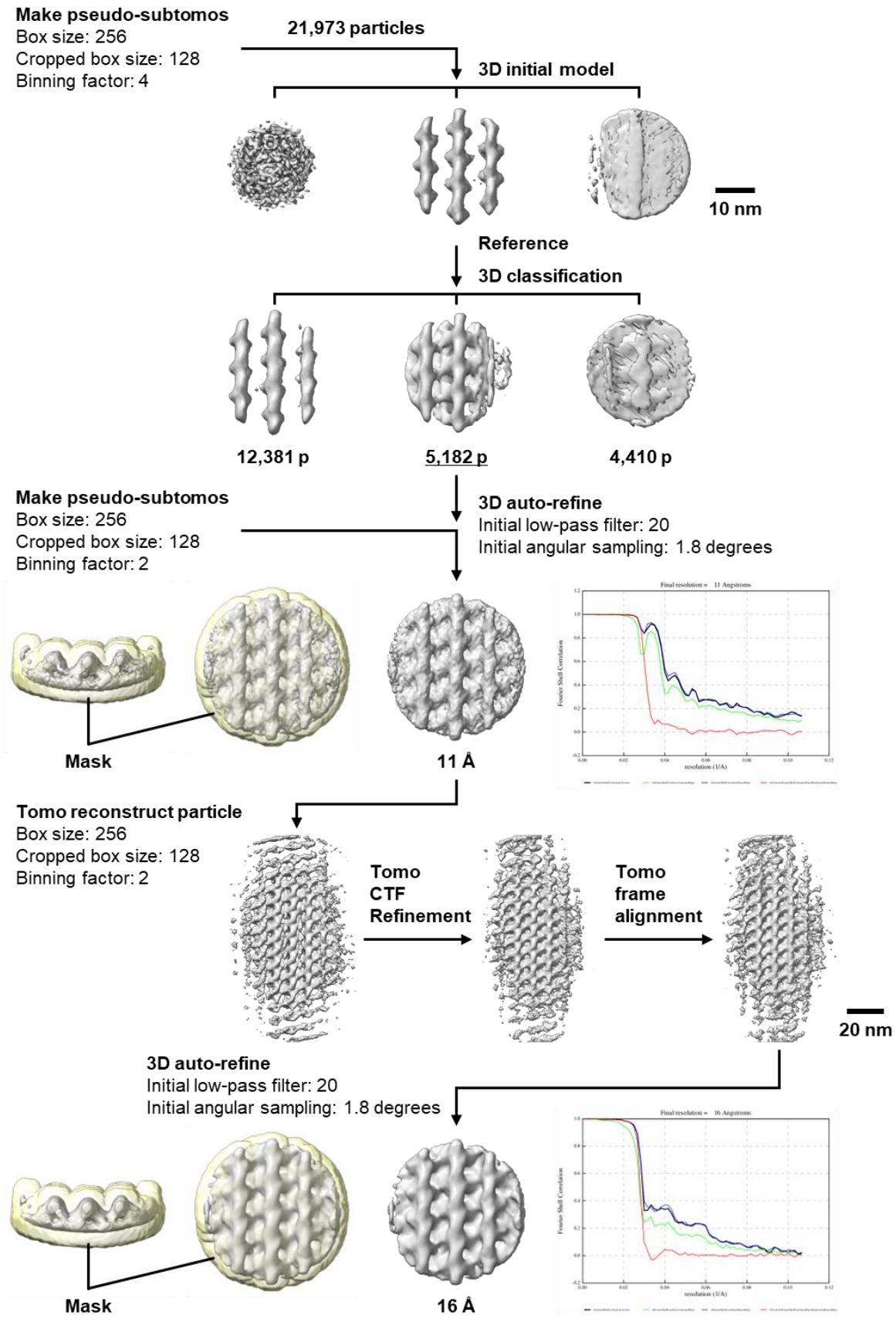

Supplementary Fig. 4-2: Workflow of cryo-ET and subtomogram averaging of the *in situ* fibril filament.

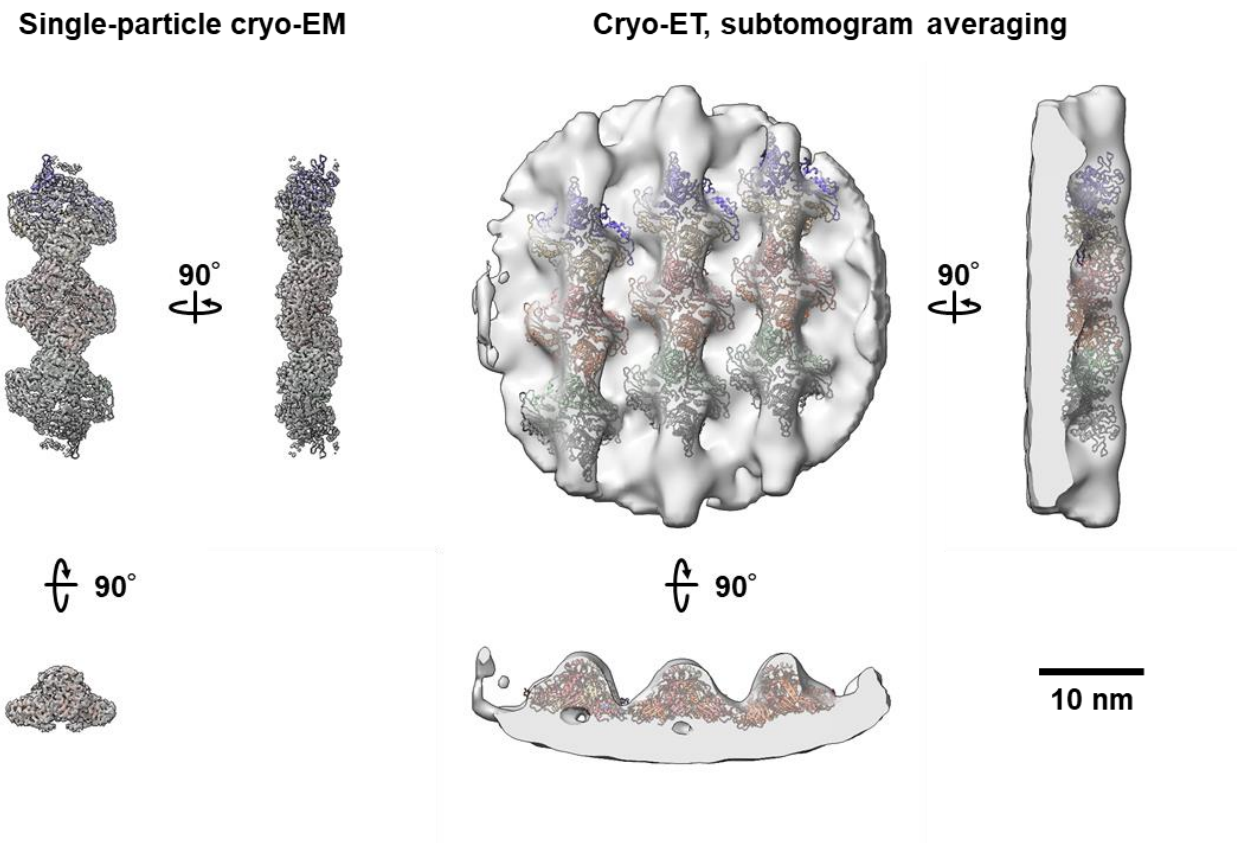

Supplementary Fig. 5: Single-particle cryo-EM structure and cryo-ET, subtomogram averaging structure of the fibril filament.
The atomic structure was fitted to each EM map. Each fibril subunit is colored differently.

GENERAL DISCUSSION

The fibril protein has been considered to be the core of the swimming motility of Spiroplasma because the fibril filament is the main component of the ribbon, the cytoskeleton and swimming machinery of Spiroplasma. However, the atomic structure of the fibril protein revealed in this study suggests that the fibril protein has lost the bacterial nucleosidase activity of evolutionary origin and that the fibril protein does not actively produce the structural changes that can drive swimming motility. Based on these results, we conclude that fibril filaments function as the basic helical skeleton of Spiroplasma cells, contributing to the cooperativity and robustness of the helicity switching in the swimming.

GENERAL CONCLUSIONS

The fibril protein is one of the most abundant proteins in *Spiroplasma* cells. It has also been considered as a major component of the internal ribbon, the unique cytoskeleton and swimming machinery of *Spiroplasma*. Therefore, the fibril protein has been isolated and performed structural analysis for a long time, but their detailed structures have remained a mystery. In this study, I succeeded in the preparation of the fibril filament suitable for structural analyses and clarified the novel atomic structure of the fibril protein by using state-of-the-art techniques such as single-particle cryo-EM, cryo-ET, and subtomogram averaging. The revealed structure of the fibril protein allowed us to discuss its evolutional origin and functional roles in the cell.

ACKNOWLEDGMENTS

I would like to express my hearty thanks to Dr. Makoto Miyata, Dr. Taro Nakamura, Dr. Ikko Fujiwara, Dr. Tasuku Hamaguchi, Dr. Toshiaki Arata, and Dr. Chikashi Shimoda at Osaka City University for their invaluable criticism and encouragement. Especially, I would like to express my deeply thanks to my supervisor Dr. Makoto Miyata for the continuous support of my PhD study and gave me many important experiences. I am deeply grateful to Dr. Keiichi Namba, Dr. Takayuki Kato, Dr. Tomoko Miyata, Dr. Akihiro Kawamoto, and Dr. Fumiaki Makino at Osaka University for giving me many knowledge and advice about Cryo electron microscopy and image analysis, and Dr. Keisuke Kawakami at Spring-8 for giving me many knowledge and advice about structural analysis. I thank Gt. Yuhei O Tahara and at Osaka City University for technical assistance with negative-staining and quick-freeze deep-etch electron microscopy, Dr. Isil Tulum at Osaka City University for gene manipulations. I really thank all members of Cell Function Laboratory for discussion and giving me a lot of invaluable ideas.

REFERENCES

1. Harne S, Gayathri P, & Beven L (2020) Exploring *Spiroplasma* biology: opportunities and challenges. *Front Microbiol* 11:589279.
2. Regassa LB & Gasparich GE (2006) Spiroplasmas: evolutionary relationships and biodiversity. *Front Biosci* 11:2983-3002.
3. Harumoto T & Lemaitre B (2018) Male-killing toxin in a bacterial symbiont of *Drosophila*. *Nature* 557(7704):252-255.
4. Nakamura S (2020) Spirochete flagella and motility. *Biomolecules* 10(4):550.
5. Miyata M*, et al.* (2020) Tree of motility - A proposed history of motility systems in the tree of life. *Genes Cells* 25(1):6-21.
6. Wada H & Netz RR (2009) Hydrodynamics of helical-shaped bacterial motility. *Phys Rev E Stat Nonlin Soft Matter Phys* 80(2 Pt 1):021921.
7. Shaevitz JW, Lee JY, & Fletcher DA (2005) *Spiroplasma* swim by a processive change in body helicity. *Cell* 122(6):941-945.
8. Grosjean H*, et al.* (2014) Predicting the minimal translation apparatus: lessons from the reductive evolution of mollicutes. *PLoS Genet* 10(5):e1004363.
9. Razin S, Yogev D, & Naot Y (1998) Molecular biology and pathogenicity of mycoplasmas. *Microbiol Mol Biol Rev* 62(4):1094-1156.
10. Claessen D & Errington J (2019) Cell wall deficiency as a coping strategy for stress. *Trends Microbiol* 27(12):1025-1033.
11. Miyata M & Hamaguchi T (2016) Integrated information and prospects for gliding mechanism of the pathogenic bacterium *Mycoplasma pneumoniae*. *Front Microbiol* 7:960.
12. Miyata M & Hamaguchi T (2016) Prospects for the gliding mechanism of *Mycoplasma mobile*. *Curr Opin Microbiol* 29:15-21.
13. Nakane D, Ito T, & Nishizaka T (2020) Coexistence of two chiral helices produces kink translation in *Spiroplasma* swimming. *J Bacteriol* 202(8):e00735-00719.
14. Harne S*, et al.* (2020) MreB5 Is a determinant of rod-to-helical transition in the cell-wall-less bacterium *Spiroplasma*. *Curr Biol* 30(23):4753-4762.e4757.
15. Roth J, Koch MD, & Rohrbach A (2018) Dynamics of a protein chain motor driving helical bacteria under stress. *Biophys J* 114(8):1955-1969.

16. Trachtenberg S*, et al.* (2008) Structure of the cytoskeleton of *Spiroplasma melliferum* BC3 and its interactions with the cell membrane. *J Mol Biol* 378(4):778-789.

17. Kürner J, Frangakis AS, & Baumeister W (2005) Cryo-electron tomography reveals the cytoskeletal structure of *Spiroplasma melliferum*. *Science* 307(5708):436-438.

18. Sasajima Y*, et al.* (2022) Isolation and structure of the fibril protein, a major component of the internal ribbon for *Spiroplasma* swimming. *Front Microbiol*:in press.

19. Liu P*, et al.* (2017) Chemotaxis without conventional two-component system, based on cell polarity and aerobic conditions in helicity-switching swimming of *Spiroplasma eriocheiris*. *Front Microbiol* 8:58.

20. Charon NW*, et al.* (2012) The unique paradigm of spirochete motility and chemotaxis. *Annu Rev Microbiol* 66:349-370.

21. Liu J*, et al.* (2009) Intact flagellar motor of *Borrelia burgdorferi* revealed by cryo-electron tomography: evidence for stator ring curvature and rotor/C-ring assembly flexion. *J Bacteriol* 191(16):5026-5036.

22. Trachtenberg S, Schuck P, Phillips TM, Andrews SB, & Leapman RD (2014) A structural framework for a near-minimal form of life: mass and compositional analysis of the helical mollicute *Spiroplasma melliferum* BC3. *PLoS One* 9(2):e87921.

23. Townsend R, Archer DB, & Plaskitt KA (1980) Purification and preliminary characterization of *Spiroplasma* fibrils. *J Bacteriol* 142(2):694-700.

24. Cohen-Krausz S, Cabahug PC, & Trachtenberg S (2011) The monomeric, tetrameric, and fibrillar organization of Fib: the dynamic building block of the bacterial linear motor of *Spiroplasma melliferum* BC3. *J Mol Biol* 410(2):194-213.

25. Shi H, Bratton BP, Gitai Z, & Huang KC (2018) How to build a bacterial cell: MreB as the foreman of *E. coli* construction. *Cell* 172(6):1294-1305.

26. Takahashi D, Fujiwara I, & Miyata M (2020) Phylogenetic origin and sequence features of MreB from the wall-less swimming bacteria *Spiroplasma*. *Biochem Biophys Res Commun* 533(4):638-644.

27. Ku C, Lo WS, & Kuo CH (2014) Molecular evolution of the actin-like MreB protein gene family in wall-less bacteria. *Biochem Biophys Res Commun* 446(4):927-932.

28. Pande V, Mitra N, Badge R, Srinivasan R, & Gayathri P (2021) Filament dynamics driven by ATP hydrolysis modulates membrane binding of the bacterial actin MreB. *BioRxiv*:10.1101/2021.1104.1108.439044.

29. Miyata M (2007) Molecular mechanism of mycoplasma gliding - a novel cell motility system. *Cell Motility*, ed Lenz P (Springer, New York), pp 137-175.

30. Miyata M & Nakane D (2013) Gliding mechanism of *Mycoplasma pneumoniae* subgroup implication from *Mycoplasma mobile*. *Molecular and Cell Biology of Mollicutes*, eds Browning G & Citti C (Horizon Press, Norfolk, UK), pp 237-252.

31. Yus E*, et al.* (2009) Impact of genome reduction on bacterial metabolism and its regulation. *Science* 326(5957):1263-1268.

32. Fraser CM*, et al.* (1995) The minimal gene complement of *Mycoplasma genitalium*. *Science* 270(5235):397-403.

33. Mizutani M & Miyata M (2019) Behaviors and energy source of *Mycoplasma gallisepticum* gliding. *J Bacteriol* 201(19):e00397-00319.

34. Kinosita Y*, et al.* (2014) Unitary step of gliding machinery in *Mycoplasma mobile*. *Proc Natl Acad Sci U S A* 111(23):8601-8606.

35. Uenoyama A & Miyata M (2005) Gliding ghosts of *Mycoplasma mobile*. *Proc Natl Acad Sci U S A* 102(36):12754-12758.

36. Takahashi D*, et al.* (2022) Structure and polymerization dynamics of bacterial actin MreB3 and MreB5 involved in *Spiroplasma* swimming. *Open Biol*:in press.

37. Gayathri P (2017) Bacterial actins and their interactors. *Curr Top Microbiol Immunol* 399:221-242.

38. Nurse P & Marians KJ (2013) Purification and characterization of *Escherichia coli* MreB protein. *J Biol Chem* 288(5):3469-3475.

39. Masson F, Pierrat X, Lemaitre B, & Persat A (2021) The wall-less bacterium Spiroplasma poulsonii builds a polymeric cytoskeleton composed of interacting MreB isoforms. *bioRxiv*.

40. Antunes A*, et al.* (2008) A new lineage of halophilic, wall-less, contractile bacteria from a brine-filled deep of the Red Sea. *J Bacteriol* 190(10):3580-3587.

41. Parveen N & Cornell KA (2011) Methylthioadenosine/S-adenosylhomocysteine nucleosidase, a critical enzyme for bacterial metabolism. *Mol Microbiol* 79(1):7-20.

42. Lee JE, Cornell KA, Riscoe MK, & Howell PL (2003) Structure of *Escherichia coli* 5'-methylthioadenosine/ S-adenosylhomocysteine nucleosidase inhibitor complexes provide insight into the conformational changes required for substrate binding and catalysis. *J Biol Chem* 278(10):8761-8770.

43. Lee JE, Cornell KA, Riscoe MK, & Howell PL (2001) Structure of *E. coli* 5'-methylthioadenosine/S-adenosylhomocysteine nucleosidase reveals similarity to the purine nucleoside phosphorylases. *Structure* 9(10):941-953.

44. Floden EW*, et al.* (2016) PSI/TM-Coffee: a web server for fast and accurate multiple sequence alignments of regular and transmembrane proteins using homology extension on reduced databases. *Nucleic Acids Res* 44(W1):W339-343.

45. Larkin MA*, et al.* (2007) Clustal W and Clustal X version 2.0. *Bioinformatics* 23(21):2947-2948.

46. Razin S & Hayflick L (2010) Highlights of mycoplasma research--an historical perspective. *Biologicals* 38(2):183-190.

47. Toyonaga T*, et al.* (2021) Chained structure of dimeric F_1-like ATPase in *Mycoplasma mobile* gliding machinery. *mBio*:e0141421.

48. Kiyama H, Kakizawa S, Sasajima Y, Tahara YO, & Miyata M (2021) Reconstitution of minimal motility system based on *Spiroplasma* swimming by expressing two bacterial actins in synthetic minimal bacterium. *bioRxiv*.

49. Distelhorst SL, Jurkovic DA, Shi J, Jensen GJ, & Balish MF (2017) The variable internal structure of the *Mycoplasma penetrans* attachment organelle revealed by biochemical and microscopic analyses: implications for attachment organelle mechanism and evolution. *J Bacteriol* 199(12).

50. Relich RF, Friedberg AJ, & Balish MF (2009) Novel cellular organization in a gliding mycoplasma, Mycoplasma insons. *J Bacteriol* 191(16):5312-5314.

51. Miyata M (2010) Unique centipede mechanism of *Mycoplasma* gliding. *Annu Rev Microbiol* 64:519-537.

52. Sasajima Y & Miyata M (2021) Prospects for the mechanism of *Spiroplasma* swimming. *Front Microbiol* 12:706426.

53. Gasparich GE (2002) *Spiroplasmas*: evolution, adaptation and diversity. *Front Biosci* 7:d619-640.

54. Trachtenberg S & Gilad R (2001) A bacterial linear motor: cellular and molecular organization of the contractile cytoskeleton of the helical bacterium *Spiroplasma melliferum* BC3. *Mol Microbiol* 41(4):827-848.

55. Trachtenberg S, Gilad R, & Geffen N (2003) The bacterial linear motor of *Spiroplasma melliferum* BC3: from single molecules to swimming cells. *Mol Microbiol* 47(3):671-697.

56. Trachtenberg S, Andrews SB, & Leapman RD (2003) Mass distribution and spatial organization of the linear bacterial motor of *Spiroplasma citri* R8A2. *J Bacteriol* 185(6):1987-1994.

57. Terahara N, Tulum I, & Miyata M (2017) Transformation of crustacean pathogenic bacterium *Spiroplasma eriocheiris* and expression of yellow fluorescent protein. *Biochem Biophys Res Commun* 487(3):488-493.

58. Uenoyama A, Kusumoto A, & Miyata M (2004) Identification of a 349-kilodalton protein (Gli349) responsible for cytadherence and glass binding during gliding of *Mycoplasma mobile*. *J. Bacteriol.* 186:1537-1545.

59. Tulum I, Tahara YO, & Miyata M (2019) Peptidoglycan layer and disruption processes in *Bacillus subtilis* cells visualized using quick-freeze, deep-etch electron microscopy. *Microscopy (Oxf)* 68(6):441-449.

60. Kawakita Y*, et al.* (2016) Structural study of MPN387, an esssential protein for gliding motility of a human-pathogenic bacterium, *Mycoplasma pneumoniae*. *J Bacteriol* 198(17):2352-2359.

61. Nakane D & Miyata M (2007) Cytoskeletal "jellyfish" structure of *Mycoplasma mobile*. *Proc Natl Acad Sci U S A* 104(49):19518-19523.

62. Zhang K (2016) Gctf: Real-time CTF determination and correction. *J Struct Biol* 193(1):1-12.

63. Zivanov J*, et al.* (2018) New tools for automated high-resolution cryo-EM structure determination in RELION-3. *Elife* 7:e42166.

64. Grant T, Rohou A, & Grigorieff N (2018) cisTEM, user-friendly software for single-particle image processing. *Elife* 7:e35383.

65. Heuser JE (2011) The origins and evolution of freeze-etch electron microscopy. *J Electron Microsc (Tokyo)* 60 Suppl 1:S3-29.

66. Williamson DL, Renaudin J, & Bove JM (1991) Nucleotide sequence of the *Spiroplasma citri* fibril protein gene. *J Bacteriol* 173(14):4353-4362.

67. Briegel A, Pilhofer M, Mastronarde DN, & Jensen GJ (2013) The challenge of determining handedness in electron tomography and the use of DNA

origami gold nanoparticle helices as molecular standards. *J Struct Biol* 183(1):95-98.

68. Jensen GJ (2015) Getting started in Cryo-EM with professor Grant Jensen. p https://www.youtube.com/watch?v=gDgFbAqdM_c.

69. Hutchison CA, 3rd*, et al.* (2016) Design and synthesis of a minimal bacterial genome. *Science* 351(6280):aad6253.

70. Lartigue C*, et al.* (2021) Tuning spherical cells into kinking helices in wall-less bacteria. *bioRxiv*.

LIST OF PUBLICATIONS AND PRESENTATIONS

PUBLICATIONS

1. **Sasajima Y**, Kato K, Miyata T, Kawamoto A, Namba K and Miyata M (2022)
   Isolation and structure of the fibril protein, a major component of the internal ribbon for *Spiroplasma* swimming. Frontiers in Microbiology. doi: 10.3389/fmicb.2022.1004601

2. **Sasajima Y** and Miyata M (2021)
   Prospects for the mechanism of *Spiroplasma* swimming.
   Frontiers in Microbiology. 12:706426. doi: 10.3389/fmicb.2021.706426

3. Mizutani M, **Sasajima Y** and Miyata M (2021)
   Force and stepwise movements of gliding motility in human pathogenic bacterium *Mycoplasma pneumoniae*. Frontiers in Microbiology. doi: 10.3389/fmicb.2021.747905

4. Takahashi D, Fujiwara I, **Sasajima Y**, Narita A, Imada K and Miyata M (2022)
   ATP-dependent polymerization dynamics of bacterial actin proteins involved in *Spiroplasma* swimming. Open Biology. doi: 10.1098/rsob.220083

5. Kiyama H, Kakizawa S, **Sasajima Y**, Tahara OY and Miyata M (2022)
   Reconstitution of a minimal motility system based on *Spiroplasma* swimming by two bacterial actins in a synthetic minimal bacterium. Science Advances. doi: 10.1126/sciadv.abo7490

PRESENTATIONS

International congress

1. ○**Yuya Sasajima**, Takayuki Kato, Tomoko Miyata, Keiichi Namba, Makoto Miyata. Mechanism of *Spiroplasma* swimming suggested by Cryo-EM structure of fibril. XXIII Biennial Congress of the International Organization for Mycoplasmology - IOM. Tel Aviv, Israel (Virtual platform), October 2021（Oral presentation）

2. ○**Yuya Sasajima**, Takayuki Kato, Tomoko Miyata, Keiichi Namba, Makoto Miyata. Mechanism of *Spiroplasma* swimming suggested by Cryo-EM structure of the fibril. BLAST XVI (Online), January 2021（Poster presentation）

3. ○**Yuya Sasajima**, Takayuki Kato, Tomoko Miyata, Keiichi Namba, Makoto Miyata. Detail structure of *Spiroplasma* fibril protein driving helicity-switching swimming with five bactarial actins. 11th Toyota Riken International Workshop on "Actin Filament: beyond the atomic resolution structures" (Nagoya), November 2019（Poster presentation）

4. ○**Yuya Sasajima**, Makoto Miyata. Internal ribbon structure driving helicity-switching swimming in *Spiroplasma*. 10th OCARINA International Symposium (Osaka), March 2019（Poster presentaion）

5. ○**Yuya Sasajima**, Isil Tulum, Makoto Miyata. Effect of MreB depolymerization on helicity-switching swimming motility in crustacean pathogen, *Spiroplasma eriocheiris*. 22nd Congress of the International Organization for Mycoplasmology - IOM, Portsmouth, New Hampshire USA, July 2018（Poster presentation）

6. ○**Yuya Sasajima**, Isil Tulum, Makoto Miyata. Effect of MreB depolymerization on helicity-switching swimming motility in crustacean pathogen, *Spiroplasma eriocheiris*. 第7回アジアマイコプラズマ学会(AOM)＆第45回日本マイコプラズマ学会(JSM)合同学会 (東京都新宿区) 2018年05月（Poster presentation）

7. ○**Yuya Sasajima**, Isil Tulum, Makoto Miyata. Effect of MreB depolymerization on helicity-switching swimming motility in crustacean pathogen, *Spiroplasma eriocheiris*. 9th OCARINA International Symposium (Osaka), March 2018（Poster presentation）

8. ○**Yuya Sasajima**, Isil Tulum, Makoto Miyata. Effect of MreB depolymerization on helicity-switching swimming motility in *Spiroplasma eriocheiris*. IGER International Symposium on Cell Surface Structures and Functions 2017, Aichi, November 2017（Poster presentation）

Domestic meeting

1. ○**笹嶋 雄也**, 加藤 貴之, 宮田 知子, 川本 晃大, 牧野 文信, 難波 啓一, 宮田 真人「電子線クライオトモグラフィーで可視化したスピロプラズマの細胞骨格リボン」第60回日本生物物理学会年会（函館市）2022年09月（ポスター発表）

2. ○**笹嶋 雄也**, 加藤 貴之, 宮田 知子, 川本 晃大, 牧野 文信, 難波 啓一, 宮田 真人「クライオ電子顕微鏡法によるスピロプラズマ細胞骨格リボンの構造解析」第22回日本蛋白質科学会年会（つくば市）2022年06月（口頭発表）

3. **〇笹嶋 雄也,** 加藤 貴之, 宮田 知子, 川本 晃大, 牧野 文信, 難波 啓一, 宮田 真人「電子線クライオトモグラフィーで可視化したスピロプラズマの細胞骨格リボン」第49回日本マイコプラズマ学会学術集会（札幌市）2022年05月（口頭発表）

4. **〇笹嶋 雄也,** 加藤 貴之, 宮田 知子, 難波 啓一, 宮田 真人「スピロプラズマのらせん反転運動機構」日本マイコプラズマ学会第48回学術集会（オンライン開催）2021年05月（口頭発表）

5. **〇笹嶋 雄也,** 加藤 貴之, 宮田 知子, 難波 啓一, 宮田 真人「クライオ EMで明らかにしたスピロプラズマ遊泳に関与するらせん状細胞骨格フィブリルの構造」第 94 回日本細菌学会総会（オンライン開催）2021 年 03 月（口頭発表）

6. **〇Yuya Sasajima**, Takayuki Kato, Tomoko Miyata, Keiichi Namba, Makoto Miyata「スピロプラズマのらせん反転機構」第 58 回日本生物物理学会年会（オンライン開催）2020 年 09 月（ポスター発表）

7. **〇笹嶋 雄也,** 加藤 貴之, 宮田 知子, 難波 啓一, 宮田 真人「スピロプラズマのらせん反転機構」日本マイコプラズマ学会第 47 回学術集会（誌上開催）2020 年 05 月

8. **〇笹嶋 雄也,** 加藤 貴之, 宮田 知子, 難波 啓一, 宮田 真人「らせん反転遊泳を駆動するスピロプラズマ“フィブリル”タンパク質の詳細構造」第 93 回日本細菌学会総会（名古屋市）2020 年 02 月（ポスター発表）

9. **〇笹嶋 雄也,** 加藤 貴之, 宮田 知子, 難波 啓一, 宮田 真人「*Spiroplasma* のらせん反転遊泳を駆動する Fibril タンパク質の詳細構造」2020 年生体運動研究合同班会議（京都市）2020 年 01 月（口頭発表）

10. **〇笹嶋 雄也,** 加藤 貴之, 宮田 知子, 難波 啓一, 宮田 真人【招待有り】「スピロプラズマの螺旋交換遊泳を駆動する内部リボン構造」日本顕微鏡学会第 62 回シンポジウム（さいたま市）2019 年 11 月（口頭発表）

11. **〇Yuya Sasajima**, Takayuki Kato, Tomoko Miyata, Keiichi Namba, Makoto Miyata スピロプラズマの螺旋交換遊泳を駆動する内部リボン構造」第 57 回日本生物物理学会年会（宮崎市）2019 年 09 月（ポスター発表）

12. **〇笹嶋 雄也,** Isil Tulum, 宮田 真人「スピロプラズマ螺旋交換遊泳運動をつかさどる内部螺旋リボン構造」第 92 回日本細菌学会総会（札幌市）

2019 年 04 月 （ポスター発表）

13. ○**Yuya Sasajima**, Isil Tulum, Makoto Miyata 「Helicity formed by actin homologs in swimming bacterium, *Spiroplasma*」 第 56 回日本生物物理学会年会 （岡山市） 2018 年 09 月 （口頭発表）

14. ○**笹嶋 雄也,** Isil Tulum**,** 宮田 真人 「Effect of MreB depolymerization on helicity-switching swimming in *Spiroplasma eriocheiris*」 第 91 回日本細菌学会総会 （福岡市） 2018 年 03 月 （ポスター発表）